

# Bulletin of the Seismological Society of America

## Estimation of earthquake early warning parameters for eastern Sicily

--Manuscript Draft--

<b>Manuscript Number:</b>	
<b>Article Type:</b>	Article
<b>Section/Category:</b>	Regular Issue
<b>Full Title:</b>	Estimation of earthquake early warning parameters for eastern Sicily
<b>Corresponding Author:</b>	Giuseppina Tusa, PhD Istituto Nazionale di Geofisica e Vulcanologia Catania, ITALY
<b>Corresponding Author's Institution:</b>	Istituto Nazionale di Geofisica e Vulcanologia
<b>Corresponding Author E-Mail:</b>	giuseppina.tusa@ingv.it
<b>Order of Authors:</b>	Giuseppina Tusa, PhD Carla Musumeci, PhD Domenico Patanè, Dr.
<b>Abstract:</b>	<p>Earthquake Early Warning Systems (EEWS) are becoming a suitable instrument for seismic risk management in real-time. In fact, they are implemented or undergoing testing in many countries around the world, since represent an effective approach to mitigate seismic risk at short time-scale. EEW systems are based on the use of relationships between some parameters measured on the initial portion of seismic signal after the onsets. Here, we address with the first approach to the implementation of EEWS in eastern Sicily, a region that has been hit by several damaging destructive earthquakes. We estimated the peak displacement amplitude of first portion of P- and S-waves, Pd, the ground-motion period parameter, <math>\tau_c</math>, and the peak ground-motion velocity, PGV, from earthquakes with <math>ML \geq 2.8</math> recorded by the broadband stations operated by the Istituto Nazionale di Geofisica e Vulcanologia. We found that the Pd is correlated with the size of earthquake and may be used to compute the magnitude for an EEW system in this area. We also derived the relationships between <math>\tau_c</math> and ML, and between Pd and PGV, which can be used to provide onsite warning in the area around a given station and evaluate the potential damaging effects. These relationships may be deemed a useful guide for the future implementation of the earthquake early warning system in the region.</p>
<b>Author Comments:</b>	<p>Dear Editor,</p> <p>Please find the paper "Estimation of earthquake early warning parameters for eastern Sicily" (authors: G. Tusa, C. Musumeci, and D. Patané) for first submission on the Bulletin of Seismological Society of America .</p> <p>Best regards Giuseppina Tusa</p> <p>July, 28, 2016</p>
<b>Suggested Reviewers:</b>	<p>Matteo Picozzi, PhD Università di Napoli 'Federico II' matteo.picozzi@unina.it He is one of the major expert of earthquake early warning at italian level.</p> <p>Alfonso Brancato, PhD Istituto Nazionale di Geofisica e Vulcanologia alfonso.brancato@ingv.it He is an expert in statistical data analysis and a very knowledgeable about the seismic activity that characterizes the eastern Sicily.</p>
<b>Opposed Reviewers:</b>	

# 1 Estimation of earthquake early warning parameters for eastern Sicily

2 Giuseppina Tusa<sup>1</sup>, Carla Musumeci<sup>1</sup>, Domenico Patanè<sup>1</sup>

3 <sup>1</sup> Istituto Nazionale di Geofisica e Vulcanologia, Italy

4 Domenico Patanè is also at Instituto Andaluz de Geofísica, Universidad de Granada, Granada,  
5 Spain

## 7 Abstract

8 Earthquake Early Warning Systems (EEWS) are becoming a suitable instrument for seismic  
9 risk management in real-time. In fact, they are implemented or undergoing testing in many  
10 countries around the world, since represent an effective approach to mitigate seismic risk at short  
11 time-scale. EEWS systems are based on the use of relationships between some parameters measured  
12 on the initial portion of seismic signal after the onsets. Here, we address with the first approach to  
13 the implementation of EEWS in eastern Sicily, a region that has been hit by several damaging  
14 destructive earthquakes. We estimated the peak displacement amplitude of first portion of P- and S-  
15 waves,  $P_d$ , the ground-motion period parameter,  $\tau_c$ , and the peak ground-motion velocity,  $PGV$ ,  
16 from earthquakes with  $M_L \geq 2.8$  recorded by the broadband stations operated by the Istituto  
17 Nazionale di Geofisica e Vulcanologia. We found that the  $P_d$  is correlated with the size of  
18 earthquake and may be used to compute the magnitude for an EEWS system in this area. We also  
19 derived the relationships between  $\tau_c$  and  $M_L$ , and between  $P_d$  and  $PGV$ , which can be used to  
20 provide onsite warning in the area around a given station and evaluate the potential damaging  
21 effects. These relationships may be deemed a useful guide for the future implementation of the  
22 earthquake early warning system in the region.

24 **Keywords:** Earthquake ground motion, earthquake early warning, seismic hazard mitigation

The structural setting of eastern Sicily is connected to the complex tectonic environment of the Central Mediterranean basin (Fig. 1a, b) which is subjected to the NNW convergence between the Eurasian and African plates and to the geodynamic processes due to the opening of the Tyrrhenian basin (Faccenna *et al.*, 2001). This tectonic setting makes the eastern Sicily one of the most hazardous zones in Italy, characterized by a significant rate of crustal seismicity. The area, in fact, has undergone some disastrous earthquakes. Among them, we can mention the ones occurring on 4 February 1169 (moment magnitude  $M_w=6.4$  by the 2011 version of the Catalogo Parametrico dei Terremoti Italiani (Rovida *et al.*, 2011), hereafter CPTI11;  $I=X$  on the MSC scale), 10 December 1542 ( $M_w=6.8$  by CPTI11;  $I=IX-X$ ), 9 and 11 January 1693 ( $M_w=6.2$  and  $7.4$  by CPTI11, respectively;  $I=IX$  and  $X-XI$ , respectively), 20 February 1818 ( $M_w=6.2$  by CPTI11;  $I=VIII-IX$ ) and on 28 December 1908 ( $M_w=7.1$  by CPTI11;  $I=X$ ), which is one of the strongest earthquakes ever to have occurred in the central Mediterranean (Boschi *et al.*, 1995). In particular, the 1693 and 1908 earthquakes completely destroyed the cities of Catania and Messina, respectively, and were followed by large tsunamis, as well. More recently, eastern Sicily has experienced minor events. In 13 December, 1990 a seismic event ( $I=VIII$ ) produced several damages in a wide area despite its magnitude  $M_s$  was equal to 5.4 (Amato *et al.*, 1995). It caused severe damage to the cities of Augusta and Catania, and 19 casualties, as well, renewing the attention in the seismic potential of eastern Sicily and the socio-political consequence of the earthquakes in the region.

In eastern Sicily, an important role is played by the volcanic area of Mt. Etna (Fig. 1a). Indeed, its seismicity creates a rather specific scenario, with relatively small earthquakes, very shallow, that can produce important damage on a local scale. The most recent examples of destructive seismic events belong to a seismic swarm (max  $M_L$  4.8) occurring at Mt. Etna in October 2002. The most damaging event of the swarm ( $M_L = 4.5$ ;  $I=VIII$ ) occurred on 29 October

50 2002 (Castello *et al.*, 2006). It struck a densely urbanized area on the southeastern flank of Mt.  
51 Etna, producing . heavy damages even to reinforced concrete structures (Azzaro *et al.*, 2006).

52 In the framework of several national projects, different research fields are supported and  
53 furthered, including earthquake hazard mitigation in eastern Sicily, as well. In particular, two  
54 closely related development projects deal with implementing an Earthquake Early Warning (EEW)  
55 system in the considered area as a tool for real-time seismic risk mitigation and management.  
56 Indeed, EEW is the current focus of considerable research effort and its potential applicability for  
57 the immediate activation of safety measures for critical systems is already undoubted (i.e., Wieland  
58 *et al.*, 2000; Sato *et al.*, 2011). As a matter of fact, the development of these systems is more related  
59 to an actual possibility to immediately trigger actions for the protection of strategic sites and  
60 lifelines rather than as an instrument giving a massive alarm to the communities (evacuating people  
61 from buildings requires warning times so long that rarely are available in urbanized areas).  
62 Moreover, due to the recent impulses on the development of earthquake early warning systems  
63 worldwide, it is significantly raising the interest toward the potential use of EEW systems for the  
64 Structural Control, adopting structure-specific applications (active and semi-active control devices)  
65 set up within the leading time so to optimize the expected structural response.

66 Over the last ten years, as a result of the technological evolution in the fields of both  
67 computing systems and data transmission, it has been possible to develop more effective techniques  
68 to analyse seismic data in real time. Indeed, the Real-Time Seismology (RTS) integrates a real time  
69 telemetry system, where the transmission of information takes place with a very low latency, with  
70 automatic processing of recorded signals, providing fast and reliable estimates of the main  
71 earthquake parameters (location, magnitude) in the first few seconds during its occurrence.

72 On the base of the configuration of the seismic network, EEW systems can be distinguished  
73 in two main types: regional and on-site (or site-specific) warning systems (Kanamori, 2005). The  
74 regional EEW systems use a dense network of seismic sensors, partially or entirely covering the  
75 area where earthquakes are likely to occur, with real-time capability to estimate the source

76 parameters (event location and magnitude) of earthquake seismic event by using the early portion of  
77 recorded seismograms. Therefore, the system uses them to predict a specific peak ground motion at  
78 distant target sites through an empirical ground-motion prediction equation. On-site EEW systems,  
79 such as the ones installed in Japan (UrEDAS, Nakamura, 1989), in California (ElarmS, Allen and  
80 Kanamori, 2003) or in Romania (Wenzel *et al.*, 1999; Böse *et al.*, 2007), are based on a single  
81 seismic station (single-station approach) or an array of seismic stations installed near the target site  
82 that needs to be alerted. After detecting the arrival of the faster but weaker P-wave, the system  
83 computes the peak amplitude and the predominant period in the very first seconds of the P waves  
84 (Wu and Kanamori, 2005a, 2005b) in order to estimate the associated peak ground motion of the  
85 more destructive S and surface waves at the target. This approach is relatively simple, but less  
86 accurate than the regional approach. It also provides smaller effective “lead-time” (e.g. the time  
87 span from the arrival of the damaging waves to the alert notification at a given target site) compared  
88 to the regional approach, which also has the advantage that the system is constantly run and tested,  
89 and the source parameter estimates gain in accuracy as more data are recorded and analysed.  
90 However, the data processing could take a lot of time that the alarm is issued after the ground  
91 motion reaches the sites of interest (defining the so-called blind zone, Kanamori, 2005). Meanwhile,  
92 regional systems are more effective to applications such as shake maps, very useful for emergency  
93 management immediately after the event (Wald *et al.*, 1999). At the same time, the site-specific  
94 EEW systems are certainly devoted to reducing the exposure of strategic facilities (lifelines,  
95 transportation infrastructures, power plants, etc.) in real-time by automated safety actions. The  
96 Ignalina nuclear power plant in Lithuania takes advantage of a site-specific EEW system (Wieland  
97 *et al.*, 2000). The seismic network, composed by six stations, is installed at 30 km from the reactor  
98 and ensures an alarm 4 - 8 s before the ground motion affects the power plant. This time is enough  
99 to activate the control rods since they need only 2 s to come into use.

100         The regional and on-site warnings can be combined to give a hybrid EEW system, by using  
101 the potential of regional seismic networks to protect different critical systems and/or the population

102 at the same time (Kanamori, 2005; Iervolino *et al.*, 2007). Wu and Kanamori (2005) experimented  
103 with the method for on-site warning based on the measure of the predominant period ( $\tau_c$ ) of initial  
104 portion of P wave by using the data recorded by accelerometric stations of the seismic network in  
105 Taiwan. Recently, Zollo *et al.* (2010) developed an integrated regional/on-site early warning  
106 method that enables estimating a Potential Damage Zone (PDZ) for the forthcoming earthquake,  
107 namely the region in which the most damage is awaited. The method is based on the estimation of  
108 the peak ground displacement ( $P_d$ ) and the predominant period ( $\tau_c$ ), in real-time, at recording sites  
109 located at increasing distances from the earthquake epicenter. An alert level is associated to each  
110 recording site on the base of critical values of  $P_d$  and  $\tau_c$ . As shown by several authors, these two  
111 early warning (EW) parameters are empirically correlated to magnitude (e.g. Wu and Kanamori,  
112 2008; Zollo *et al.*, 2010; Colombelli *et al.*, 2012; Carranza *et al.*, 2013) and to peak ground velocity  
113 and acceleration (e.g. Böse *et al.*, 2007; Zollo *et al.*, 2010; Carranza *et al.*, 2013).

114 In this work, we determine the two EW parameters,  $P_d$  and  $\tau_c$ , together with the peak ground  
115 velocity,  $PGV$ , by using a set of more than 200 seismic events and explore the use of  $P_d$  and  $\tau_c$   
116 parameters for EEW purposes in the studied area. The aim is to compute specific empirical  
117 relationships of these two parameters with earthquake size and peak ground motion parameters for  
118 future applications of an EEW system in eastern Sicily. An example of the practical application of  
119 the obtained results are performed by the software platform PRESTo (Probabilistic and  
120 Evolutionary early warning SysTem, see Data and Resources) by Satriano *et al.* (2011) in  
121 simulation mode (from the playback of the actual recorded waveforms). PRESTo integrates  
122 algorithms for real-time, rapid earthquake location, magnitude estimation and damage assessment.  
123 The code is currently being tested in southern Italy on the Irpinia Seismic Network (ISNet).

124

125 Dataset and record processing

126 Seismic hazard in eastern Sicily is linked to earthquakes occurring in different  
127 seismotectonic areas and associated with various types of faulting mechanisms. This should ensure  
128 that the effects due to rupture directivity and focal mechanism on peak amplitudes are averaged out.

129 The eastern part of the Sicily is mainly characterized by two active volcanic regions, the  
130 Aeolian Archipelago lying in the southern Tyrrhenian Sea and the Mount Etna located in the central-  
131 eastern Sicily. From a seismological point of view, the northern Sicily and its Tyrrhenian off-shore  
132 are characterized by the activity of different tectonic structures associated both to the collision  
133 between European and African Plates, and the opening of Tyrrhenian Basin. The seismicity is  
134 mainly located in the hinge zone between southern Tyrrhenian and northern Sicily, and is confined  
135 in two principal hypocentral sectors (Gueguen *et al.*, 2002; Giunta *et al.*, 2009). The deep seismicity  
136 is essentially connected to the subduction processes of the Ionian lithospheric slab beneath the  
137 Calabrian arc and affects the northeastern Sicily. Instead, the shallow seismicity represents the  
138 expression of the strain crossing the whole orogeny (Neri *et al.*, 1996).

139 Etnean seismic events share their signatures with earthquakes recorded in the near tectonic  
140 environments of the Hyblean Plateau and Peloritani-Calabrian Arc (Patanè *et al.*, 1997; Patanè and  
141 Giampiccolo, 2004). The regional tectonic stresses together with the local stresses connected to the  
142 magma migration in the earth's crust, provide the necessary energy for rock failure.

143 The local surface tectonic structures on Mt. Etna, are connected to an intense superficial  
144 seismic activity, essentially characterized by earthquakes often clustered in swarms and having  
145 focal depths generally less than 3 km (Patanè *et al.*, 2004). Although the shallowest events  
146 characterize the most central-eastern portion of the volcano, they affect the entire volcanic area,  
147 albeit less in number. Occurring in particular geological conditions, they are considered to form a  
148 family of events whose characteristic hypocentral location has effects on both seismic scaling laws  
149 and wave propagation phenomena. This complex tectonic situation raises questions on the  
150 homogeneity of the parent population and on the treatment of the data as a whole. Therefore, we did  
151 not include in the analysis any shallow events ( $H \leq 5$  km) occurring in the Mount Etna area. So doing

152 we reduce the introduction of heterogeneities in the data set. The selected data set consists of 232  
153 crustal seismic events (Figure 2) recorded between 2006 and 2014 by the stations of the “*Rete*  
154 *Sismica Permanente della Sicilia Orientale*” (RSPSO) operated by *Istituto Nazionale di Geofisica e*  
155 *Vulcanologia (INGV) Sezione di Catania– Osservatorio Etneo* (Fig. 1c). The seismic network is  
156 located in a region between the Hyblean Plateau and the volcanic archipelago of Aeolian Islands,  
157 and comprises about eighty digital stations equipped with Nanometrics Trillium broadband  
158 seismometers having an eigenperiod of 40 s. The signals are digitized at each station with 24-bit  
159 resolution at 100 samples/s.

160 The seismic events considered in the analyses have been extracted from the “Catalogo dei  
161 terremoti della Sicilia Orientale - Calabria Meridionale, INGV, Catania” (Gruppo Analisi Dati  
162 Sismici, 2016) within an area defined by the rectangle of latitude N 35.90 – 38.85 and longitude E  
163 13.45 – 16.85, local magnitude ( $M_L$ ) greater than 2.8 (maximum  $M_L=4.8$ ; about 35% of the  
164 earthquakes have a magnitude  $\geq 3.5$ ) and focal depth up to 35 km (Fig. 2). We have chosen this  
165 interval of magnitude for the quality of data and homogeneity of the instrumental chain. The  
166 seismic events were located by using the Hypoellipse code (Lahr, 1989) in a seven layer, one-  
167 dimensional velocity structure (Hirn *et al.*, 1991). A constant  $V_p/V_s$  ratio of 1.73 for travel time  
168 calculations was assumed. Figure 3a shows the distribution of records of our data set with respect to  
169 local magnitude and hypocentral distance. The starting data set has hypocentral distances from 6 to  
170 377 km. However, the 99% of total data have been acquired at a distance less than about 200 km,  
171 therefore by considering a range up to this distance we obtain a spatial sampling rather  
172 homogeneous and dense. Looking at Figure 3a, we can expect that no bias is introduced, since no  
173 evident trend between magnitude and hypocentral distance exists. Finally, Figure 3b shows the  
174 signal-to-noise (S/N) ratio for the P phases estimated over windows of 2 s wide. It evidences that  
175 the 97% of windows have an S/N ratio greater than 5 dB, therefore suggesting a good quality of our  
176 data set.



177 As a first step in the processing, the data were checked visually at all stations to exclude  
178 traces with electronic glitches, and with phenomena of amplitude saturation. The digitized velocity  
179 time histories of the three components of ground motion were first baseline corrected, by removing  
180 the offset and the linear trends, and thus instrument corrected. Therefore, we identified the P-phases  
181 and their picks on the unfiltered vertical velocity components. As a final step, we integrated the  
182 velocity records to obtain the displacement time series and, in order to remove the low frequencies  
183 introduced by numerical integration, a high-pass Butterworth filter with corner frequency of 0.075  
184 Hz was applied to the data.

## 185 186 Empirical correlation laws for eastern Sicily

### 187 *Peak ground displacement, magnitude and distance*

188 Nakamura (1984, 1988), with the EEW system known as UrEDAS, was the pioneer in  
189 considering the first few seconds of recorded P-waves to estimate the magnitude of a seismic  
190 event. The method of Nakamura consists in computing continually in real-time the predominant  
191 period from the first 2 to 4 s of P waves for estimating the magnitude of the event. An alternative  
192 technique has been proposed by Wu and Zhao (2006), based on the use of the peak displacement  
193 amplitude,  $P_d$ , measured on the three seconds window starting from the P-wave arrival time  
194 picking. They investigated the relationship between  $P_d$ , the hypocentral distance and the local  
195 magnitude in southern California and Taiwan . They found that  $P_d$  can be used to estimate the  
196 magnitude of seismic events and can have a practical application in the EEW system.  
197 Independently, Zollo *et al.* (2006, 2007) showed that the peak displacement amplitude of first few  
198 seconds of P- and S-wave seismic signal scales with the earthquake magnitude for  $4 \leq M_w \leq 7$ ; it can  
199 be used for the estimation in real-time of the earthquake size in EEW applications. Two important  
200 differences distinguish the approach by Zollo *et al.* (2006, 2007) from that by Wu and Zhao (2006):  
201 (1) the time window is not fixed to three seconds and (2) the initial S-waves are taken into account,  
202 as well. Indeed, when a dense seismic network is placed around the potential source area, the S-

phases data, which are available at the stations closest to the epicenter, can be used to improve the magnitude estimation before the strong ground shaking reaches the distant target sites.

Following Lancieri and Zollo (2008), P- ( $P_dP$ ) and S-waves ( $P_dS$ ) peak displacement amplitudes are measured on the modulus of displacement defined as:

$$D = \sqrt{Z^2 + EW^2 + NS^2} \quad (1)$$

where Z, EW and NS are the vertical, east-west and north-south components of ground motion, respectively. Unlike P-waves picking, the onset of S-waves has been estimated from travel time of P waves by assuming a ratio  $V_p/V_s = 1.73$  ( $V_p$  and  $V_s$  are the P- and S- wave velocities, respectively). Therefore, we measure  $P_d$  on time windows of 2 s and 4 s of P-waves (denoted as  $2P$  and  $4P$ , respectively) and 2 s for the S-wave (denoted as  $2S$ ) starting from the P- and S-waves picked arrivals.

The logarithmic  $P_d$  is generally assumed to be related to magnitude ( $M$ ) and hypocentral distance ( $R$ ) through the standard attenuation expression ( Wu and Zhao, 2006; Zollo *et al.*, 2006; Lancieri and Zollo, 2008):

$$\text{Log}_{10}(P_d) = a + bM + c\text{Log}_{10}(R) \quad (2)$$

where  $b$  and  $c$  are the coefficients describing the magnitude dependence and the exponent in the distance dependent amplitude decay (that is the geometrical attenuation, assumed constant in all the investigated distance range), respectively. The model in equation (2) does not include the term representing the anelastic attenuation, that is the linear R term. This is generally removed from the model since it was found not to be statically significant (Wu and Zhao, 2006). Before testing this assumption for our data, we need to make a number of points which emerge from the distribution of

228  $\log_{10}(P_d)$  as a function of hypocentral distance. In Figure 4 the  $\log_{10}(P_d)$  measured on time  
 229 windows of 2 s (2P and 2S) and 4 s (4P) are plotted versus the hypocentral distance for three narrow  
 230 ranges of magnitude, 2.8-3.0, 3.6-3.8, and 4.6-4.8, respectively. So doing we reduce the scatter in  $P_d$   
 231 amplitudes due to the different source sizes. At distances less than about 60 km, essentially  
 232 corresponding to attenuation of direct waves and where the effect of the anelastic attenuation should  
 233 be smaller, the  $\log_{10}(P_d)$  values decay at a rate higher than those shown by  $\log_{10}(P_d)$  values at  
 234 larger distances, for all three considered magnitude intervals. In fact, beyond about 60 km the rate  
 235 of decay of the  $\log_{10}(P_d)$  is less severe due to the arrival of energy refracted and reflected from the  
 236 deeper parts of the crust. This means that if we consider a wide range of hypocentral distance, the  
 237 coefficient  $c$  in equation (2) cannot be supposed constant. Therefore, in order to estimate the  
 238 relationship between peak ground displacement, local magnitude, and distance, only records with a  
 239 maximum hypocentral distance of 60 km have been used. The number of records considered thus  
 240 drops to 3,928 three-component seismograms. This choice is also based on the general observation  
 241 that the crustal seismic events have high-frequency direct body waves with dominant amplitude at  
 242 distance from the receiver comparable with earthquake rupture length (Zeng *et al.*, 1993). Figure 5  
 243 describes the distribution of the number of three component seismograms as a function of  
 244 magnitude that we used to perform the further analysis.

245 We investigate the attenuation due to geometrical spreading and anelastic attenuation  
 246 reformulating the equation of  $\log_{10}(P_d)$  as follows

$$\log_{10}(P_d) = a + bM + c\log_{10}(R) + dR \quad (3)$$

249  
 250 where  $dR$  represents the anelastic attenuation. In Table 1, the regression coefficients, together with  
 251 their 95% confidence interval, for 2P, 4P, and 2S are reported for both attenuation models. Note that  
 252  $P_d$  is in meters and  $R$  is in kilometers. The coefficient of elastic attenuation,  $d$ , was found not to be  
 253 statically significant, with a positive value very close to zero. Additionally, its introduction in the

254 attenuation model does not improve the fit of the data as evidenced by the root mean squared errors  
255 and the coefficient of determination values (see Table 1 A and B for comparison). It was therefore  
256 removed from the model.

257 A residual analysis has been performed in order to verify whether the regression models are  
258 able to explain as much variation as possible in the dependent variable, assuming that the random  
259 error is uniquely distributed over the data set. In particular, the regression analysis can be  
260 considered successful in explaining the variation of the dependent variable if the residuals are  
261 unstructured and small. Otherwise, the validity of regression is questionable since the residuals are  
262 correlated to two independent variables. Figure 6 (a, b, and c) shows the residuals as a function of  
263 the hypocentral distance and magnitude. It is clear from the figure that the residuals do not show  
264 any significant trends both vs. magnitude and hypocentral distance. Additionally, more than about  
265 90% of residuals is in the range  $-0.5 \div 0.5$  for the three considered time windows.

266 The equation (2) has been used to correct for the distance effects the observed peak  
267 amplitudes, by normalizing them to a reference distance of 30 km, a value chosen since  
268 approximates the mean epicentral distance for the considered data set. As shown in Figure 7, there  
269 is an evident positive correlation between the logarithmic peak displacement normalized to 30 km  
270  $[Log_{10}(P_d)^{30km}]$  and the local magnitude for 2P, 4P, and 2S time windows in the whole investigated  
271 magnitude range.

272 For each magnitude value, we first calculated the mean and the standard deviation of  
273  $Log_{10}(P_d)^{30km}$  for both P- and S-waves. Therefore, a linear regression line was computed for the  
274 means of  $Log_{10}(P_d)^{30km}$  weighted by the inverse of standard deviation ( $\sigma$ ) as (Zollo *et al.*, 2006):

275

$$276 \quad Log_{10}(P_d)^{30km} = a' + b' M \quad (4)$$

277

278 The means of  $\text{Log}_{10}(P_d)^{30km}$  are shown in the Figure 7 (black dots), whilst the estimated coefficients  
 279  $a'$  and  $b'$  are listed in Table 2, together with the calculated weighted standard errors (WSE) that has  
 280 been computed as:

281

$$282 \quad WSE = \sqrt{\frac{\sum_i w_i [\text{Log}_{10}(P_{di})^{30km} - (a' + b' M_i)]^2}{\sum_i w_i}} \quad (5)$$

283

284 where  $w_i = 1/\sigma_i$  for the  $i^{th}$  value of magnitude. The peak amplitudes are log linearly correlated with  
 285 magnitude in the considered magnitude range ( $2.8 \leq M_L \leq 4.8$ ) for both P- and S-waves, with  
 286 correlation coefficients greater than 0.98 even for very short time windows from P-wave arrivals.

287

#### 288 $\tau_c$ and magnitude

289 Nakamura (1988) was the first to develop a method for rapidly estimating the magnitude of  
 290 an earthquake for early warning purposes by using the frequency content of the first P-wave train.  
 291 Nakamura's approach is based on the computation of the predominant period for the first P-wave  
 292 train taking into account the vertical component of ground-motion. It has been widely applied to  
 293 data from both broad-band and strong-motion stations in several seismic regions, demonstrating that  
 294 the predominant period scales with seismic event magnitude (Allen and Kanamori, 2003; Olson and  
 295 Allen, 2005; Lockman and Allen, 2007), and up to a few hundreds of kilometers from the seismic  
 296 source is independent from the epicentral distance (Allen and Kanamori, 2003; Allen *et al.*, 2009a,  
 297 b).

298 An alternative method has been developed by Wu and Kanamori (2005a), based on the  
 299 computation of the characteristic period,  $\tau_c$ , defined as:

300

$$\tau_c = 2\pi \sqrt{\frac{\int_0^{\tau_0} u^2(t)dt}{\int_0^{\tau_0} v^2(t)dt}} \quad (6)$$

where  $u(t)$  and  $v(t)$  are the ground-motion displacement and velocity, respectively. The time window of integration starts at the P wave onset time and has a duration equal to  $\tau_0$ , generally set a 3 s.  $\tau_c$  is considered to represent the average period of P-wave signal and several studies have shown that it reflects the sizes of earthquakes (Kanamori, 2005; Wu and Kanamori, 2005b). Moreover,  $\tau_c$  is less affected by the filter parameters and pre-event noise than the predominant period for the first P-wave train, since it is estimated on the actual P-wave window (Shieh *et al.*, 2008).

For the estimation of  $\tau_c$ , we considered the ground motion filtered (high-pass filtered at 0.075 Hz) displacement,  $u(t)$ , and velocity,  $v(t)$ , from the vertical component of ground motion.  $\tau_0$  has been set to 3 s.

In the model considered here, the parameter  $\tau_c$  is depending only on the source characteristics and not on the distance. In order to verify this assumption, we plot in Figure 8a the  $\tau_c$  as a function of the hypocentral distance. Looking at the figure, we observe that  $\tau_c$  does not show any significant trend with the distance, at least up to 60 km, as further confirmed by t-test with significance threshold equal to 0.05.

As before, a linear regression was estimated for the means of  $\text{Log}_{10}(\tau_c)$  computed for each value of magnitude (Fig. 8b), weighted by the inverse of standard deviation. It has the following equation:

$$\text{Log}_{10}(\tau_c) = 0.143(\pm 0.070)M_L - 0.853(\pm 0.266) \quad (7)$$

324 where  $\tau_c$  is measured in seconds, suggesting that the average  $\text{Log}_{10}(\tau_c)$  values increase with  
 325 increasing magnitude. The uncertainties associated to the two coefficients of the model are the 95%  
 326 confidence intervals. In Figure 9, we compare our relationship with those obtained by Zollo *et al.*  
 327 (2010) considering the data from south of Italy, Taiwan, and Japan, and Carranza *et al.* (2013) with  
 328 data from the south of the Iberian Peninsula, SE Iberia and north Africa. The regression through our  
 329 data yielded similar results to the findings of Zollo *et al.* (2010), even though the investigated  
 330 ranges of magnitude are different, whilst the relationship by Carranza *et al.* (2013) suggests a closer  
 331 dependence of the period parameter  $\tau_c$  on the magnitude. These differences could be attributed to  
 332 the characteristics of the used dataset. In particular, Zollo *et al.* (2010) selected waveform records of  
 333 events essentially occurring at a depth less than 50 km and acquired at less than 60 km hypocentral  
 334 distance, as in our case. However, their magnitude range spanned 4 to 8.5. Conversely, Carranza *et al.*  
 335 (2013) considered seismic events with magnitude ranging from 3.8 to 5.9 but recorded at  
 336 regional distances (up to 700 km).

337

### 338 *Peak ground velocity, PGV, versus $P_d$*

339 Wu and Kanamori (2005a) showed that  $P_d$  is correlated with the peak ground-motion  
 340 velocity,  $PGV$ , at the same site, and when  $P_d > 0.5$  cm, the event is most likely able to produce  
 341 damages. Therefore, in real-time, the measured  $P_d$  and  $\tau_c$  can be used to calculate the level of  
 342 shaking (that is  $PGV$ ) at the target sites, and  $M$ , respectively, even though  $M$  is not directly used for  
 343 onsite early warning purposes.

344 In Figure 10, the  $PGV$  values, measured as the maximum amplitude between the two  
 345 unfiltered horizontal components of ground motion velocity, are plotted as a function of peak  
 346 displacement  $P_d$ , measured from the low-pass filtered displacement records over a 3 s time window  
 347 after the P-wave pick. The figure shows that overall the  $PGV$  values increase logarithmically with  
 348  $P_d$  in the investigated range of magnitude, in agreement with findings of several previous studies

349 (e.g., Wu *et al.*, 2007; Zollo *et al.*, 2010). Again, considering a maximum distance of 60 km, we  
350 obtain the following best-fit regression line:

351

$$352 \quad \log_{10}(PGV) = 1.36(\pm 0.05) + 0.91(\pm 0.02)\log_{10}(P_d) \quad (8)$$

353

354 where the units of  $PGV$  are cm/s and of  $P_d$  are cm. The standard deviation of  $\log_{10}(PGV)$  is 0.27,  
355 whilst the coefficient of determination is 0.80. In Figure 11, we compare our  $PGV$ - $P_d$  relationship  
356 against others calibrated for several areas worldwide by Wu *et al.* (2007), Zollo *et al.* (2010), and  
357 Carranza *et al.* (2013). The comparison suggests that our data distribution is consistent with the  
358 empirical regression lines obtained by these authors, independently of the considered maximum  
359 distance and magnitude ranges.

360

## 361 Discussion

362 We have estimated empirical scaling relationships between the EEW parameters,  $P_d$  and  $\tau_c$ ,  
363 and both magnitude and peak ground velocity ( $PGV$ ), by using the broadband velocity seismograms  
364 of earthquakes occurring in eastern Sicily. The data have been acquired by the stations of the  
365 currently operating network in the area whose distribution ensures a good distance and azimuthal  
366 coverage (Fig. 1c), making this case study a good test for the application of EEW methodologies.

367 The  $\tau_c$ - $M_L$  empirical scaling law estimated with our data distribution proved very similar  
368 with that obtained by Zollo *et al.* (2010) by using strong motion data recorded in south of Italy,  
369 Taiwan, and Japan in spite of the differences in the magnitude ranges covered by the data (see Fig.  
370 9). The estimated  $PGV$  versus  $P_d$  relationship is nearly identical to those obtained from data of  
371 various regions around the world (see Fig. 11). This suggests that, despite the scatter of the data  
372 around the mean, the correlation between  $PGV$  and  $P_d$  is independent of effects such as source,  
373 attenuation, site response or tectonic regime (Zollo *et al.*, 2010; Carranza *et al.*, 2013). The



374 uncertainty bounds associated to the regression lines take into account the potential differences due  
375 to the regional context or earthquake mechanisms.

376 In order to understand how the estimated scaling laws work, we selected some events that  
377 are not included in the dataset used to discover the predictive relationships, as test data. In  
378 particular, we considered 20 events ranging from magnitude  $M_L$  2.8 to 4.3 (see Table 3) and  
379 compared the observed  $P_d$ ,  $\tau_c$ , and  $PGV$  values with the predicted ones. In Figure 12, we compare  
380 the base-10 logarithms of observed  $P_d$  ( $P_{d-obs}$ ) values for 2P, 4P, and 2S time windows with the  
381 predicted  $P_d$  ( $P_{d-pred}$ ) by equation (2). We note that there is a general decreasing trend of  $P_d$  values  
382 with the hypocentral distance. This was to be expected because of the combined effect of the  
383 geometrical spreading and anelastic attenuation on the amplitude peak ground motion. Figure 12  
384 shows that the  $P_{d-pred}$  accords well with the observed one, since the data points are well aligned  
385 along the straight line with slope equal to 1.

386 The comparison between the average of the observed  $\tau_c$  values and the predicted ones by  
387 equation (7) for the 20 earthquakes belonging to the test dataset is shown in Figure 13, where the  
388 range of one standard deviation is also reported. Taking into account the uncertainty of magnitude  
389 estimation (on average  $\pm 0.2$  units), as well, we can see that the average of the observed  $\tau_c$  values  
390 are within the predictive uncertainty bounds ( $\pm 1SVD$ ).

391 Finally, we compare the predicted and observed  $PGV$  of the 20 test events in Figure 14,  
392 where the  $45^\circ$  line is also shown. It can be seen that the data are distributed fairly close to the  $45^\circ$   
393 line, suggesting that the values determined by the equation (8) are reliable estimates of  $PGV$ . For  
394 example, for the two earthquakes of  $M_L=3.5$  (see Table 3), equation (8) predicts  $Log_{10}(PGV)$  (with  
395  $PGV$  in cm/s) from -2.3 to -0.9 with a mean value of  $-1.8 \pm 0.26$ . Within the uncertainty, these values  
396 are consistent with the observed  $Log_{10}(PGV)$  from -2.5 to -0.9, with a mean of  $-1.8 \pm 0.31$ . Similarly,  
397 for the events in Table 3 with  $M_L=4.1$  the  $Log_{10}(PGV)_{pred}$  estimates from -1.6 to -0.1 (mean equal to  
398  $-1.0 \pm 0.4$ ) accord well with the  $Log_{10}(PGV)_{obs}$  from -1.8 to -0.1 (mean equal to  $-0.9 \pm 0.4$ ). These

399 results confirm the robustness of  $P_d$  as a predictor of  $PGV$  for regional earthquake monitoring  
400 purposes and EEW operations in our region.

401 An example of application of the obtained results in terms of EEW in the studied area has  
402 been performed by the software platform PRESTo in simulation mode. It is mainly based on the  
403 RTLoc (Satriano *et al.*, 2008) and RTMag (Lancieri and Zollo, 2008) algorithms for the earthquake  
404 location and magnitude estimation in real-time, respectively. As regards the code, we do not go into  
405 details here and refer the reader to the original paper by Satriano *et al.* (2011). It is worth noting that  
406 the module RTMag implemented inside PRESTo makes use of empirical correlation laws between  
407  $\text{Log}_{10}(P_d)$  and magnitude, such as equation 3. Playing back the recorded traces into PRESTo we can  
408 to follow up the accuracy of the earthquake parameter predictions through the estimated empirical  
409 laws and, at the same time, we can evaluate the speed of convergence for both location and  
410 magnitude estimates for a potential development of EEW system in the investigated area.

411 As a case study, we present a simulation of a  $M_L$  4.6 (23 June 2011) earthquake, one of the  
412 strongest events in our dataset. It occurred close to the village of Tortorici (see star in Fig. 2), at  
413 about 45 km away from a key refinery in Milazzo. Looking at the plots in Figure 15, we can  
414 quantitatively analyse the results of the computation and see how quickly the system produces  
415 reliable and stable estimation of the event parameters on the basis of the information coming from  
416 the actual seismic network. The first input parameters are the P-phase picks that are required by the  
417 phase association algorithm and the location module. In particular, before declaring an event at least  
418 3 picks within 5 s must be acquired by the system. This condition is reached 5.09 s after the event  
419 origin time (Fig. 15b), when the stations MUCR, MSFR, and ECAN trigger. 0.2 s later, the first  
420 location is available with a difference of about 8 km with respect to the reference epicentral location  
421 and focal depth (namely the one from the seismic catalog). At the same time, the first magnitude  
422 estimate is 5.0 with an uncertainty (Fig. 15a), defined as the confidence interval between 5% and  
423 95%, from 3.6 to 7.5. This estimation is associated to the 2P window available at the nearest station  
424 (MUCR, at about 8 km from the epicenter). At 6.2 s from the origin, another 2P window is available

425 (at station MSFR) and the estimated magnitude reaches 4.0 with smaller error (from 3.7 to 5.2,  
 426 range that still contains the true value). As more  $P_d$  measurements are acquired by the system, the  
 427 magnitude estimates through the empirical regression model is more and more refined and the  
 428 uncertainty decreases. In fact, at about 8 s (15 P picks) from the origin time the magnitude settles at  
 429 4.6, with an error equal to  $\pm 0.4$  units of magnitude, which is reasonable for an early warning  
 430 application. Therefore, with the actual network configuration, both location and magnitude  
 431 estimations are fairly stable and reliable after about 8 s from the origin time, when the system gives  
 432 awaited lead times equal to 7 s at Milazzo, 13 s at Catania and 14 s at Messina. This means that  
 433 when the event is declared the expected lead times are about 3 s longer.

434 In the platform PRESTo the on-site approach to EEW is addressed through the threshold-  
 435 based method by Zollo *et al.* (2010) for the independent definition of alert levels at each recording  
 436 sites. This approach has the advantage that the potential damaging effects of the earthquake are  
 437 evaluated without requiring accurate real-time location of the event. This is particularly useful when  
 438 the distribution of the stations is very sparse and does not guarantee an optimal azimuthal coverage  
 439 to obtain an early and reliable location of the epicenter. In the threshold approach, the parameters  $P_d$   
 440 and  $\tau_c$ , measured in a 3 s time window after the first P-arrival time at each station, are compared  
 441 with a priori selected threshold values that define four alert levels (from 0 to 3, see Zollo *et al.*,  
 442 2010 for details) inside a decisional table. These levels are connected to both the expected on-site  
 443 damages and the damages at distance. Considering a threshold value of macroseismic intensity  $I_{MCS}$   
 444 (Mercalli-Cancani-Sieberg Intensity Scale) for damage effects equal to VII, we can estimate the  
 445 PGV expected by using the regression relationships by Faenza and Michelini (2010). Note that the  
 446 MCS Intensity scale is used in Italy to describe the effects of the earthquake ground shaking on the  
 447 built environment and communities. For  $I_{MCS}=VII$  the Faenza and Michelini (2010) empirical law  
 448 predicts  $PGV = 6$  cm/s, that we can convert into  $P_d$  threshold value by using the equation (8) and  
 449 taking 1 standard deviation, obtaining  $P_d = 0.1$  cm. The  $\tau_c$  threshold can be estimated through the  
 450 equation (7) for a minimum magnitude value fixed as threshold. On the basis of seismic history of

the region, we selected  $M_L$  5, estimating a  $\tau_c = 0.3$  s obtained, again considering a 1 standard deviation. Figure 16 shows the time evolution of  $P_d$  and  $\tau_c$  measurements for the  $M_L$  4.6 seismic event we considered above, and the alert levels that have been associated to the recording sites. The first measurements of  $P_d$  and  $\tau_c$  are available after 6.1 s from the origin time, or after 3.1 s from the first P-pick at station MUCR which is the nearest station to the epicenter. According to  $P_d$  and  $\tau_c$  values, the system associates an alert level 3 (damage expected nearby and far from stations, Zollo *et al.* (2010)) since at MUCR both measurements are higher than the threshold values. The values of  $\tau_c$  remain stable with time (or with distance) (Fig. 16a) and consistent from one station to another. Conversely,  $P_d$  shows a decreasing trend with time or distance, as expected, and the values rapidly drop under the threshold value (alert level 1) (Fig. 16c). In this case study, only at station MUCR the threshold values are reached and surpassed. On the contrary, if there are a certain number of near source stations where  $P_d$  and  $\tau_c$  exceed the threshold values, the real-time mapping of alert levels can be used to predict the Potential Damage Zone (PDZ) (Zollo *et al.*, 2010). This is particularly important to guarantee an efficient planning of rescue operations during emergency phases immediately after an earthquake.

466

#### 467 Concluding remarks

Today, the development of earthquake early warning systems represents one of the most useful strategy to mitigate seismic risk in short time-scales and many countries worldwide are promoting and developing such systems. In the frame of seismic risk management, it is considered a reasonable costly solution for the loss reduction. Additionally, the developments of the real time seismology are opening new scenarios in the framework of interaction of EEW and earthquake engineering applications (i.e., Fujita *et al.*, 2011; Kubo *et al.*, 2011; Maddaloni *et al.*, 2011; Nakamura *et al.*, 2011).

475           The great number of data we used in this study, acquired by the current seismic network  
476 deployed in eastern Sicily, ensured an appropriate sample size for the robustness and accuracy of  
477 the empirical laws we estimated. This is an important aspect since the reliability of the predicted  
478 ground shaking depends, first of all, on the accuracy of the attenuation law applied to estimate it.  
479 Moreover, with its present configuration, the network can be useful for evaluating how to develop  
480 the seismic early warning system and select the most appropriate approach (regional, on-site, or  
481 mixed) for the area. For instance, it is dense enough to allow the PRESTo platform to converge to a  
482 stable estimation of the location and magnitude 2 to 3 s from the event declaration.

483           Evaluating the practicability of an EEW system in this area is justified by its high level of  
484 seismic hazard. Moreover, three big oil refineries and power plants are installed along the eastern  
485 coast of Sicily in the cities of Milazzo, Augusta and Priolo Gargallo, which have as main activity the  
486 refining of crude oil and its derivatives. For them suitable safety measures such as, for example, the  
487 automatic blocking of pipelines or gas lines in order to prevent fire hazards or the automatic  
488 shutdown of the manufacturing operations to avoid the equipment casualty, could be adopted for the  
489 damage reduction. Therefore, the introduction of an EEW system within the practices of frame of  
490 real-time seismology that has been regularly carried out for years in eastern Sicily is a worthwhile  
491 objective, since it can be effectively used to reduce damage caused by strongest earthquakes.

492           Taking into account the distribution of the major earthquakes in eastern Sicily, it could be  
493 expected that in many cases the regional approach will not give enough time to process the data and  
494 divulgate the alarm. Some problems may arise, above all, for the events occurring offshore. For  
495 them, more coastal stations might be needed to better constrain the earthquake location. However,  
496 for these events the on-site threshold-based EEWs approach can issue an alert rapidly to the in-land  
497 target sites and estimate a potential damage zone within very few seconds (2-3 s) from the origin of  
498 the seismic event, increasing the lead-time and reducing the blind zone.

499           In conclusion, hopefully it will be the development in eastern Sicily of a seismic network  
500 that includes the real-time processing of the seismic recordings since it can be used also as a tool to

501 predict in real-time the ground motion measure and allow emergency response to be carried out  
502 quickly.

503

#### 504 Data and Resources

505 Seismic recordings used in this work are not accessible to the public. The Web site for the software  
506 PRESTo is [www.prestoews.org](http://www.prestoews.org) (last accessed March 2015).

507

#### 508 Acknowledgements

509 This work has been supported by the following projects: VULCAMED “Potenziamento strutturale  
510 di centri di ricerca per lo studio di aree VULCANICHE ad alto rischio e del loro potenziale  
511 geotermico nel contesto della dinamica geologica e ambientale MEDiterranea” and SIGMA  
512 “Sistema Integrato di sensori in ambiente cloud per la Gestione Multirischio Avanzata”, inside the  
513 2007-2013 infrastructural Italian Program PON (Programma Operativo Nazionale, Ricerca e  
514 Competitività - Asse I: “Sostegno ai mutamenti strutturali”); “Attività di sviluppo sperimentale  
515 finalizzata alla riduzione del rischio sismico nella Sicilia Orientale” inside the PO-FESR 2007-2013  
516 Sicilia; MED-SUV funded from the European Union Seventh Framework Programme (FP7) under  
517 Grant agreement n°308665. Our work benefited from the support by Stephen Conway for the  
518 language correction.

519

#### 520 References

521 Allen, R. M. (2007). The ElarmS earthquake early warning methodology and application  
522 across California, In *Earthquake Early Warning System*, P. Gasparini, G. Manfredi, J. Zschau (Eds),  
523 Springer, p. 21-44.

524 Allen, R. M., and H. Kanamori (2003). The potential for earthquake early warning in  
525 Southern California, *Science*, **300**, 786-789.

Allen, R. M., H. Brown, M. Hellweg, O. Khainovski, P. Lombard, and D. Neuhauser (2009a). Real-time earthquake detection and hazard assessment by ElarmS across California, *Geophys. Res. Lett.*, **36**, L00B08, doi: 10.1029/2008GL036766.

Allen, R. M., P. Gasparini, O. Kamigaichi, and M. Böse (2009b). The status of earthquake early warning around the world: an introductory overview, *Seism. Res. Lett.*, **80**, doi: 10.1785/gssrl.80.5.682.

Amato, A., R. Azzara, A. Basili, C. Chiarabba, M. Cocco, M. Di Bona, and G. Selvaggi (1995). Main shock and aftershocks of the December 13, 1990 Eastern Sicily earthquake. *Ann. Geophys.*, **38**, 255-266.

Azzaro, R., S. D'Amico, A. Mostaccio, L. Scarfi, and T. Tuvè (2006). Terremoti con effetti macrosismici in Sicilia orientale nel periodo gennaio 2002-dicembre 2005. *Quad. Geofis.* **41**, INGV, Roma (in Italian).

Boschi, E., G. Ferrari, P. Gasperini, E. Guidoboni, G. Smriglio, and G. Valensise (1995), Catalogo Dei Forti Terremoti in Italia Dal 461 A. C. Al 1980, Ist. Naz. di Geofis., Rome.

Böse, M., C. Ionescu, and F. Wenzel (2007). Earthquake early warning for Bucharest, Romania: novel and revised scaling relations, *Geophys. Res. Lett.*, **34**, L07302, doi: 10.1029/2007GL029396.

Carranza, M., E. Bufon, S. Colombelli, and A. Zollo (2013). Earthquake early warning for southern Iberia: a P wave threshold-based approach, *Geophys. Res. Lett.*, **40**, 4588-4593.

Castello B., G. Selvaggi, C. Chiarabba, and A. Amato (2006). CSI Catalogo della sismicità italiana 1981-2002, versione 1.1. INGV-CNT, Roma. <http://www.ingv.it/CSI/>

Colombelli, S., A. Zollo, G. Festa, and H. Kanamori (2012). Early magnitude and potential damage zone estimates for the great  $M_w$  9 Tohoku-Oki earthquake, *Geophys. Res. Lett.*, **39**, L22306, doi: 10.1029/2012GL053923.

Espinosa-Aranda, J. M., A. Jimenez, G. Ibarrola, F. Alcantar, and A. Aguilar (1995). Mexico City seismic alert system, *Seism. Res. Lett.*, **66**, 42-53.

552 Faccenna, C., T. W. Becker, F. P. Lucente, L. Jolivet, and F. Rossetti (2001). History of  
553 subduction and back-arc extension in the Central Mediterranean, *Geophys. J. Int.*, **145**, 809-820.

554 Faenza, L., and A. Michelini (2010). Regression analysis of MCS intensity and ground  
555 motion parameters in Italy and its application in ShakeMap, *Geophys. J. Int.*, **180**, 1138-1152.

556 Gueguen, E., E. Tavarnelli, P. Renda, and M. Tramutoli (2002). The geodynamics of the  
557 southern Tyrrhenian Sea margin as revealed by integrated geological, geophysical and geodetic  
558 data. *Boll. Soc. Geol. It.*, **1**, 77-85.

559 Heaton, T. H. (1985). A model for a seismic computerized alert network, *Science*, **229**, 987-  
560 990.

561 Fujita, S., K. Minagawa, H. Shimosaka, and G. Tanaka (2011). Intelligent seismic isolation  
562 system using air bearings and earthquake early warning, *Soil Dyn. Earth. Eng.*, **31**, 223-230.

563 Hirn, A., A. Nercessian, M. Sapin, F. Ferrucci, G. Wittlinger (1991). Seismic heterogeneity  
564 of Mt. Etna: structure and activity, *Geophys. J. Int.*, **105**, 139–153.

565 Kanamori, H. (2005). Real time seismology and earthquake damage mitigation, *Ann. Rev.*  
566 *Earth Planet Sci.*, **33**, 195-214.

567 Kubo, T., Y. Hisada, M. Murakami, F. Kosuge, and K. Hamano (2011). Application of an  
568 earthquake early warning system and a real-time strong motion monitoring system in emergency  
569 response in a high-rise building, *Soil Dyn. Earth. Eng.*, **31**, 231-239.

570 Lahr, J. C. (1989). HYPOELLIPSE/VERSION 2.0: A computer program for determining  
571 local earthquake hypocentral parameters, magnitude, and first motion pattern, *U.S. Geol. Surv.*  
572 *Open File Rep.*, 89/116, 81 pp.

573 Lancieri, M., and A. Zollo (2008). A bayesian approach to the real-time estimation of  
574 magnitude from the early P and S wave displacement peaks, *J. Geophys. Res.*, **113**, B12302, doi:  
575 10.1029/2007JB005386.

576 Lockman, A., and R. M. Allen (2005). Single station earthquake characterization for early  
577 warning, *Bull. Seism. Soc. Am.*, **95**, 2029-2039.



578 Lockman, A., and R. M. Allen (2007). Magnitude-period scaling relations for Japan and the  
579 Pacific Northwest: implications for earthquake early warning, *Bull. Seism. Soc. Am.*, **97**, 140-150.

580 Maddaloni, G., N. Caterino, and A. Occhiuzzi (2011). Semi-active control of the benchmark  
581 highway bridge based on seismic early warning systems, *Bull. Earth. Eng.*, **9**, 1703-1715.

582 Musumeci, C., L. Scarfi, M. Palano, and D. Patanè (2014). Foreland segmentation along an  
583 active convergent margin: New constraints in southeastern Sicily (Italy) from seismic and geodetic  
584 observations, *Tectonophysics*, **630**, 137-149, doi: 10.1016/j.tecto.2014.05.017.

585 Nakamura, Y. (1984). Development of the earthquake early-warning system for the  
586 Shinkansen, some recent earthquake engineering research and practical in Japan. The Japanese  
587 National Committee of the International Association for Earthquake Engineering, 224-238.

588 Nakamura, Y. (1988). On the urgent earthquake detection and alarm system (UrEDAs),  
589 *Proceedings of the 9<sup>th</sup> World Conference on Earthquake Engineering*, Tokyo-Kyoto, Japan.

590 Nakamura, Y., J. Saita, and T. Sata (2011). On a earthquake early warning system (EEW)  
591 and its applications, *Soil Dyn. Earth. Eng.*, **31**, 127-136.

592 Neri, G., D. Caccamo, O. Cocina, and A. Montalto (1996). Geodynamic implications of  
593 earthquake data in the Southern Tyrrhenian Sea. *Tectonophysics*, **258**, 233-249.

594 Patanè, D., O. Cocina, S. Falsaperla, E. Privitera and S. Spampinato (2004). Mt Etna  
595 Volcano: A Seismological Framework. In: "Etna Volcano Laboratory", Bonaccorso A., Calvari S.,  
596 Coltelli M., Del Negro C., Falsaperla S. (Eds), AGU (Geophysical monograph series), 147-165.

597 Olson, E., and R.M. Allen (2005). The deterministic nature of earthquake rupture, *Nature*,  
598 **438**, 212-215.

599 Patanè, D. and E. Giampiccolo (2004). Faulting processes and earthquake source parameters  
600 at Mount Etna: State of the Earth and perspectives, In: A. Bonaccorso, S. Calvari, M. Coltelli, C.  
601 Del Negro and S. Falsaperla (eds.), Etna Volcano Laboratory, AGU Geophysical monograph series,  
602 167-189.

603           Rovida, A., R. Camassi, P. Gasperini, and M. Stucchi (eds.) (2011). CPTI11, the 2011  
604 version of the Parametric Catalogue of Italian Earthquakes. Istituto Nazionale di Geofisica e  
605 Vulcanologia, Milano, Bologna. doi: <http://doi.org/10.6092/INGV.IT-CPTI11>.

606           Sato, S., K. Ashiya, S. Yamamoto, N. Iwata, M. Korenaga, and S. Noda (2011). Practical  
607 use of the Earthquake Early Warning (EEW) system for Shinkansen, *Proceedings of the 9<sup>th</sup> World*  
608 *Congress on Railway Research*, Lille, France.

609           Satriano, C., A. Lomax, and A. Zollo (2008). Real-time evolutionary earthquake location for  
610 seismic early warning, *Bull. Seism. Soc. Am.*, **98**, 1482-1494, doi: 10.1785/01200601590.

611           Satriano, C., L. Elia, C. Martino, M. Lancieri, and A. Zollo (2011). PRESTo, the earthquake  
612 early warning system for southern Italy: concepts, capabilities and future perspectives, *Soil Dyn.*  
613 *Earth. Eng.*, **21**, 137-153.

614           Selvaggi, G. and C. Chiarabba (1995). Seismicity and P-wave velocity image of the  
615 Southern Tyrrhenian subduction zone. *Geophys. J. Int.*, **121**, 818-826, doi: 10.1111/j.1365-  
616 246X.1995.tb06441.x

617           Shieh, J., Y.M. Wu, and R. Allen (2008). A comparison of  $\tau_c$  and  $\tau_{max}^p$  for magnitude  
618 estimation in earthquake early warning, *Geophys. Res. Lett.*, **35**, L20301, doi:  
619 10.1029/2008GL035611.

620           Wieland, M., M. Gresser, and C. Kuendig (2000). Seismic early warning system for a  
621 nuclear power plant, *Proceedings of the 12<sup>th</sup> World Conference on Earthquake Engineering*,  
622 Auckland, New Zeland.

623           Wu, Y. M., and H. Kanamori (2005a). Rapid assessment of damage potential of earthquakes  
624 in Taiwan from the beginning of P waves, *Bull. Seism. Soc. Am.*, **95**, 1181-1185.

625           Wu, Y. M., and H. Kanamori (2005b). Experiment on an onsite early warning method for  
626 the Taiwan early warning system, *Bull. Seism. Soc. Am.*, **95**, 347-353.

627           Wu, Y. M., and L. Zhao (2006). Magnitude estimation using the first three seconds P-wave  
628 amplitude in earthquake early warning, *Geophys. Res. Lett.*, **33**, L16312,

629 doi:10.1029/2006GL026871

630 Wu, Y. M., H. Y. Yen, L. Zhao, B. S. Huang, and W. T. Liang (2006). Magnitude  
631 determination using initial *P* waves: a single-station approach, *Geophys. Res. Lett.*, **33**, L05306,  
632 doi:10.1029/2005GL025395.

633 Wu, Y.M., H. Kanamori, R. M. Allen, and E. Hauhsson (2007). Determination of earthquake  
634 early warning parameters,  $\tau_c$  and  $P_d$ , for southern California, *Geophys. J. Int.*, **170**, 711-717, doi:  
635 10.1111/j.1365-246X.2007.03430.x.

636 Wu, Y. M., and H. Kanamori (2008). Development of an earthquake early warning system  
637 using real-time strong motion signals, *Sensors*, **8**, 1-9.

638 Zeng, Y., K. Aki, and T. Teng (1993). Mapping of the high-frequency source radiation for  
639 the Loma Prieta Earthquake, California. *J. Geophys. Res.*, **98**, 11,981-11,993.

640 Zollo, A., M. Lancieri, S. Nielsen (2006). Earthquake magnitude estimation from peak  
641 amplitudes of very early seismic signals on strong motion records, *Geophys. Res. Lett.*, **33**, L23312,  
642 doi:10.1029/2006GL027795.

643 Zollo, A., M. Lancieri, S. Nielsen (2007). Reply to comment by P. Rydelek et al. on  
644 “Earthquake magnitude estimation from peak amplitudes of very early seismic signals on strong  
645 motion records”, *Geophys. Res. Lett.*, **34**, L20303, doi:10.1029/2007GL030560.

646 Zollo, A., O. Amoroso, M. Lancieri, Y. M. Wu, and H. Kanamori (2010). A threshold-based  
647 earthquake early warning using dense accelerometer networks, *Geophys. J. Int.*, **183**, 963-947.

648

649

650

651

652

653

654

655

Tables

**Table 1** - Coefficients of equations 2 and 3 for the prediction of  $\text{Log}_{10}(\text{P}_d)$ .

Equation 2										
	a	CI95 for a	b	CI95 for b	c	CI95 for c	d	CI95 for d	RMSE	R <sup>2</sup>
<b>2P</b>	-5.865	0.115	0.990	0.022	-1.915	0.068	-	-	0.3231	0.7140
<b>4P</b>	-5.904	0.239	1.007	0.026	-1.860	0.142	-	-	0.3151	0.7331
<b>2S</b>	-5.437	0.109	1.069	0.023	-2.016	0.062	-	-	0.3395	0.7331
Equation 3										
<b>2P</b>	-5.442	0.324	0.991	0.022	-2.327	0.303	0.0057	0.004	0.3228	0.7146
<b>4P</b>	-5.735	1.620	1.007	0.026	-2.004	1.378	0.0015	0.014	0.3152	0.7331
<b>2S</b>	-5.425	0.246	1.069	0.023	-2.028	0.233	0.0002	0.003	0.3396	0.7332

CI95 indicates the confidence intervals at 95% confidence level.

RMSE indicates the root mean squared errors.

R<sup>2</sup> is the coefficient of determination.

656

**Table 2** - Coefficients of equation 3 for the prediction of  $\text{Log}_{10}(\text{P}_d)^{30\text{km}}$ .

	a'	CI95 for a'	b'	CI95 for b'	WSE	R <sup>2</sup>
<b>2P</b>	-8.817	0.216	1.024	0.057	0.078	0.982
<b>4P</b>	-8.757	0.205	1.036	0.054	0.077	0.984
<b>2S</b>	-8.494	0.227	1.092	0.060	0.086	0.982

CI95 indicates the confidence intervals at 95% confidence level.

RMSE indicates the root mean squared errors.

R<sup>2</sup> is the coefficient of determination.

657

658

659

660

661

662

**Table 3** - List of events used as test dataset.

Date (yyyy/mm/dd)	Time (hh:min:ss)	Latitude (°)	Longitude (°)	Depth (km)	M <sub>L</sub>
2013/11/05	05.06.39.880	37.709	14.919	15.6	2.9
2014/01/01	01.59.50.610	36.644	14.954	8.9	3.0
2014/04/17	21.52.25.630	38.207	15.216	14.3	2.8
2014/06/27	02.56.47.770	37.803	14.590	18.6	3.1
2014/10/09	22.58.26.540	38.485	14.730	14.5	4.3
2014/10/10	16.27.12.920	38.056	15.105	33.1	2.9
2014/10/22	22.41.51.740	38.473	14.799	17.3	3.1
2015/01/05	07.27.02.830	37.167	15.289	20.8	3.1
2015/02/08	19.39.21.980	37.339	15.195	19.0	2.9
2015/02/11	03.57.00.110	38.034	14.754	9.3	3.1
2015/08/08	22.46.24.960	38.458	14.272	11.5	4.1
2015/09/20	22.27.59.120	37.170	15.507	21.9	4.1
2015/10/09	00.35.29.540	37.729	15.115	6.6	3.0
2015/10/10	21.37.44.980	37.839	14.879	22.9	2.8
2015/12/20	09.46.07.470	38.354	13.892	32.4	4.3
2015/12/22	05.35.09.180	37.773	15.431	21.8	3.5
2016/02/08	15.35.42.720	37.002	14.802	6.0	4.3
2016/02/08	17.57.37.320	37.002	14.806	6.0	3.6
2016/02/11	01.38.50.520	37.835	15.376	30.0	3.5
2016/03/01	16.47.50.470	38.490	14.613	12.4	3.1

663

664

665

666

## 667 **Figure captions**

668

669 **Figure 1.** (a, b) Simplified tectonic map (after Musumeci *et al.*, 2014). (c) Geographic  
670 distribution of the permanent stations of the “*Rete Sismica Permanente della Sicilia Orientale*”  
671 (RSPSO).

672 **Figure 2.** Epicentral map of the 232 earthquakes selected for this study. The green star  
673 indicates the event used to perform the test with the code PRESTo (see text for details).

674 **Figure 3.** (a) Plot of local magnitude ( $M_L$ ) vs. hypocentral distance for the whole data set  
675 shown in Figure 2; (b) histogram showing the signal-to-noise ratio (dB) of P-waves used for the  
676 analysis ( $\sim 7000$ ).

677 **Figure 4.** Plots of peak displacement amplitude versus hypocentral distance for three  
678 different range of magnitude.

679 **Figure 5.** Number of 3C seismograms vs. local magnitude for the data set used to solve  
680 equation 2 (see text for details).

681 **Figure 6.** Distribution of residuals of the  $\text{Log}_{10}(P_d)$  as a function of the independent  
682 variables hypocentral distance and local magnitude for the three time windows (2P, 4P, and 2S).

683 **Figure 7.** Logarithm of  $P_d$  parameter normalized at a reference distance of 30 km versus the  
684 local magnitude (a and b) in the time windows 2s and 4s from the P-onset and (c) 2s from the S-  
685 onset (grey diamonds). Black dots indicate the mean of  $\text{Log}_{10}(P_d)^{30km}$  for each  $M_L$  value plotted with  
686 its standard deviation. The solid and dashed lines indicate the best fit and  $\pm 1WSE$  error bounds,  
687 respectively.

688 **Figure 8.** (a) The  $\tau_c$  parameter versus hypocentral distance. (b) Correlation between the  
689 logarithm of period parameter  $\tau_c$  value and local magnitude (grey diamonds). Black dots indicate  
690 the mean of  $\text{Log}_{10}(\tau_c)$  for each local magnitude value plotted with its standard deviation. The best fit  
691 regression line (solid line), along with  $\pm 1WSE$  error bounds (dashed lines), is shown.  $R$  is the  
692 correlation coefficient.

693 **Figure 9.**  $\tau_c$ -magnitude relations obtained from this study, from Zollo *et al.* (2010), and  
694 Carranza *et al.* (2013). The grey area indicates the  $\pm 1SDV$  error bounds.

695 **Figure 10.** Peak ground velocity ( $PGV$ ) versus peak initial displacement amplitude ( $P_d$ ) for  
696 hypocentral distances up to 60 km. Solid and dashed lines show the least squares fit and the range  
697 of one standard deviation, respectively.  $R$  is the correlation coefficient and  $SDV$  is the standard  
698 deviation.

699 **Figure 11.** Comparison of  $PGV$ - $P_d$  relationship obtained in this study with those estimated  
700 by Wu *et al.* (2007) (data from Taiwan and Southern California), Zollo *et al.* (2010) (data from  
701 Italy, Japan, and Taiwan), and Carranza *et al.* (2013) (data from south of Iberian Peninsula).

702 **Figure 12.** (Left) Plots of observed values of  $\log_{10}(P_d)$  versus the hypocentral distance.  
703 (Right) Plots of predicted values of  $\log_{10}(P_d)$  versus the observed ones (the line 1:1 is also shown)  
704 from the three time windows (2P, 4P, and 2S) for the 20 selected events (see also Table 3) of the  
705 test dataset.

706 **Figure 13.** The observed  $\tau_c$  parameter versus the local magnitude ( $M_L$ ) for the 20 seismic  
707 events belonging to the test dataset. The predicted  $\tau_c$  (black line) by equation (7) and  $\pm 1SDV$  (black  
708 dashed lines) are also shown.

709 **Figure 14.** Predicted  $PGV$  ( $PGV_{pred}$ ) versus observed  $PGV$  ( $PGV_{obs}$ ) for the 20 selected  
710 events of test dataset (see text for details). The line 1:1 is also shown.

711 **Figure 15.** PRESTo timeline for the  $M_L$  4.6, 23 June 2011 earthquake occurring near the  
712 village of Tortorici. The dashed line in the plots (a) and (f) represent the reference magnitude and  
713 focal depth, respectively, obtained from the seismic catalog.

714 **Figure 16.** Evolution in time of the ground parameters (a)  $\tau_c$ , (b)  $P_d$ , and (c) the  
715 corresponding alert level at the different stations for the  $M_L$  4.6, 23 June 2011 earthquake as  
716 estimated by the code PRESTo.

717

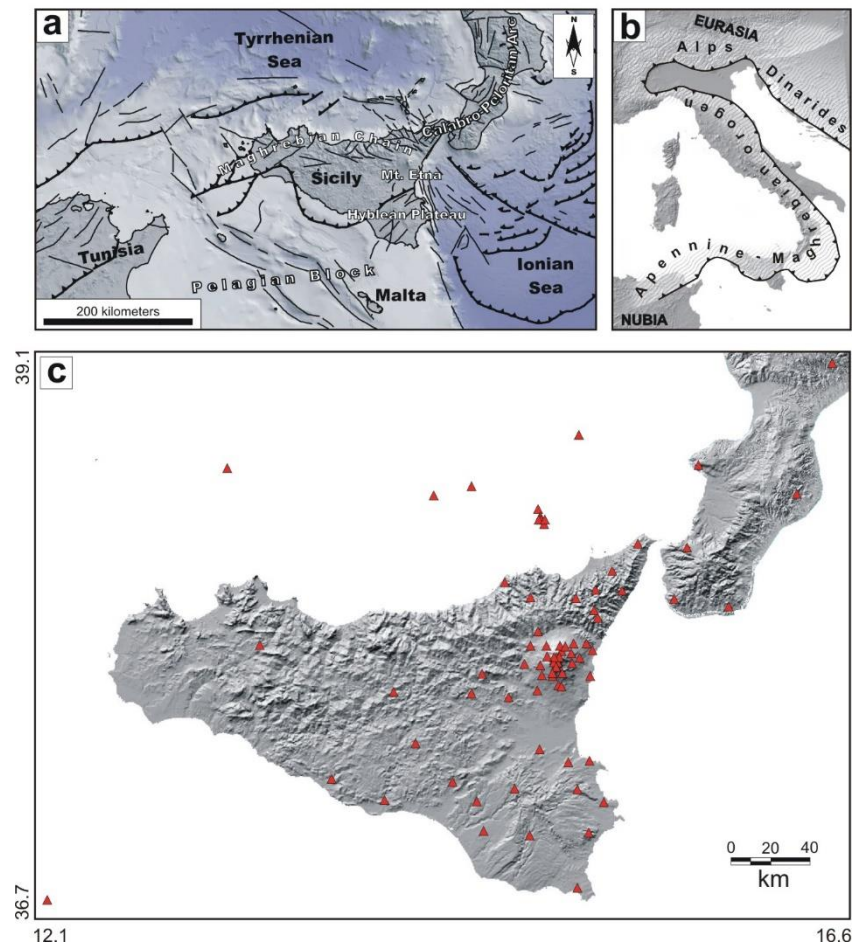


**Figure 1.** (a, b) Simplified tectonic map (after Musumeci *et al.*, 2014). (c) Geographic distribution of the permanent stations of the “*Rete Sismica Permanente della Sicilia Orientale*” (RSPSO).



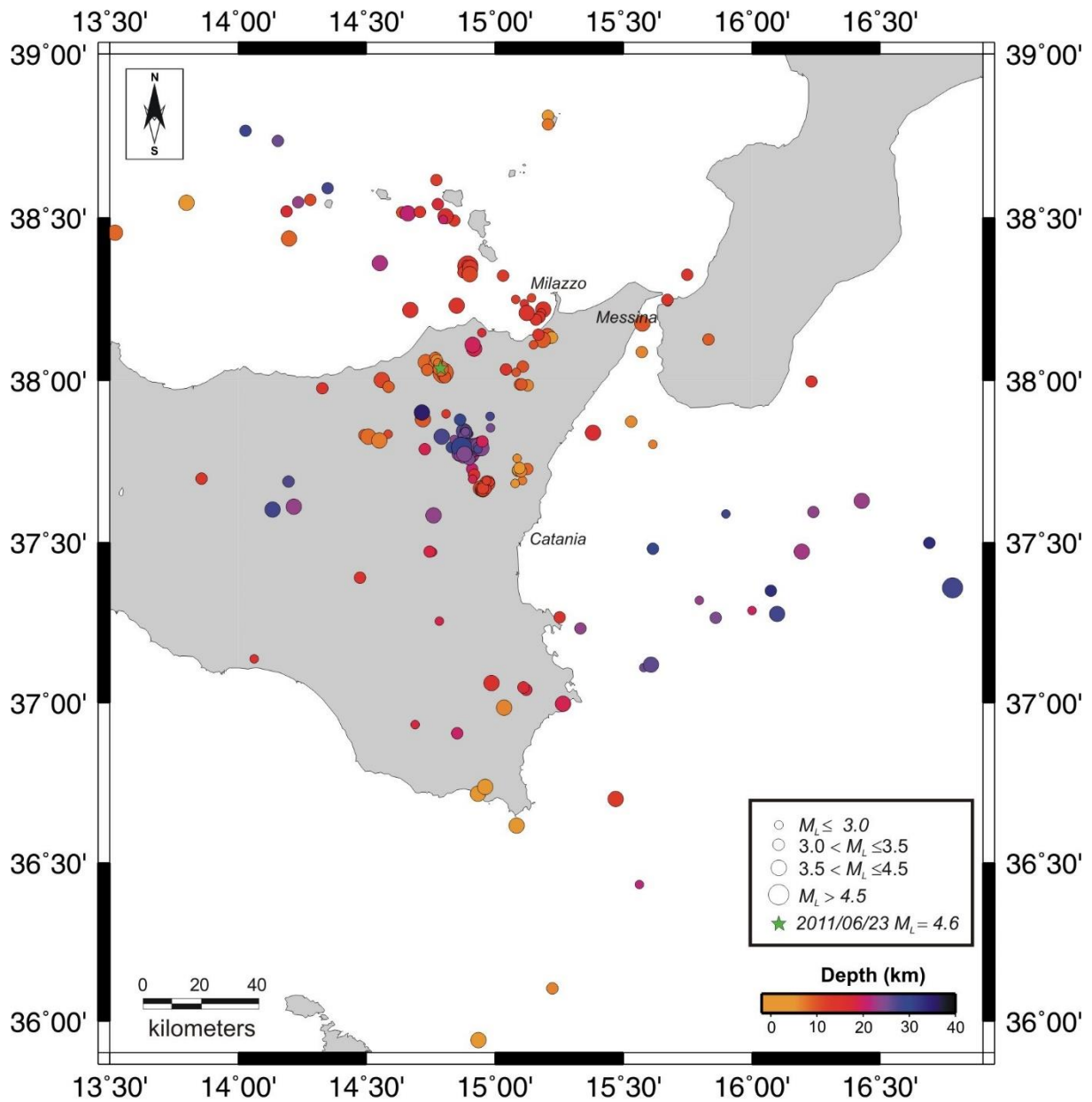


**Figure 2.** Epicentral map of the 232 earthquakes selected for this study. The green star indicates the event used to perform the test with the code PRESTo (see text for details).

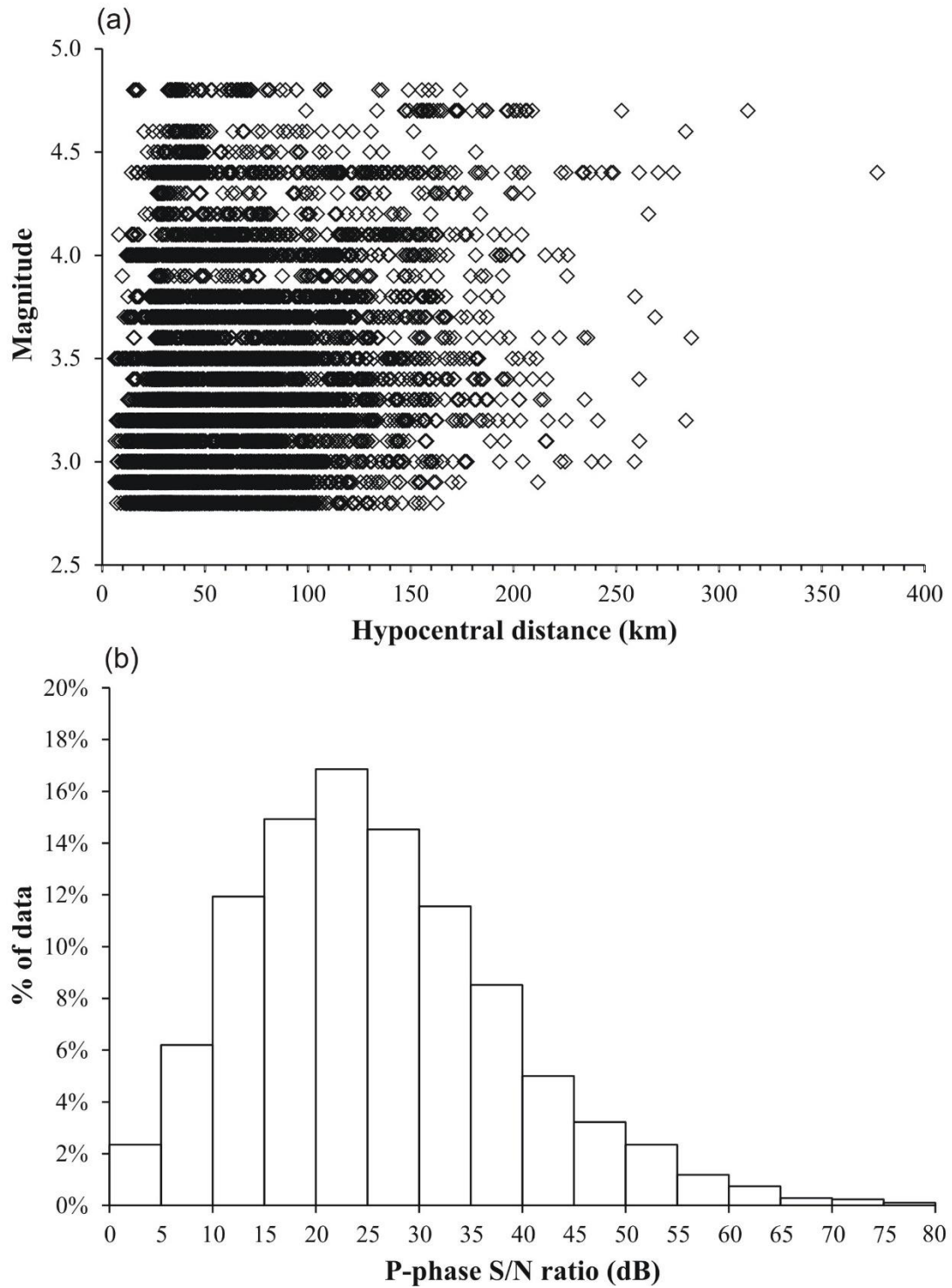


**Figure 3.** (a) Plot of local magnitude ( $M_L$ ) vs. hypocentral distance for the whole data set shown in Figure 2; (b) histogram showing the signal-to-noise ratio (dB) of P-waves used for the analysis (~7000).

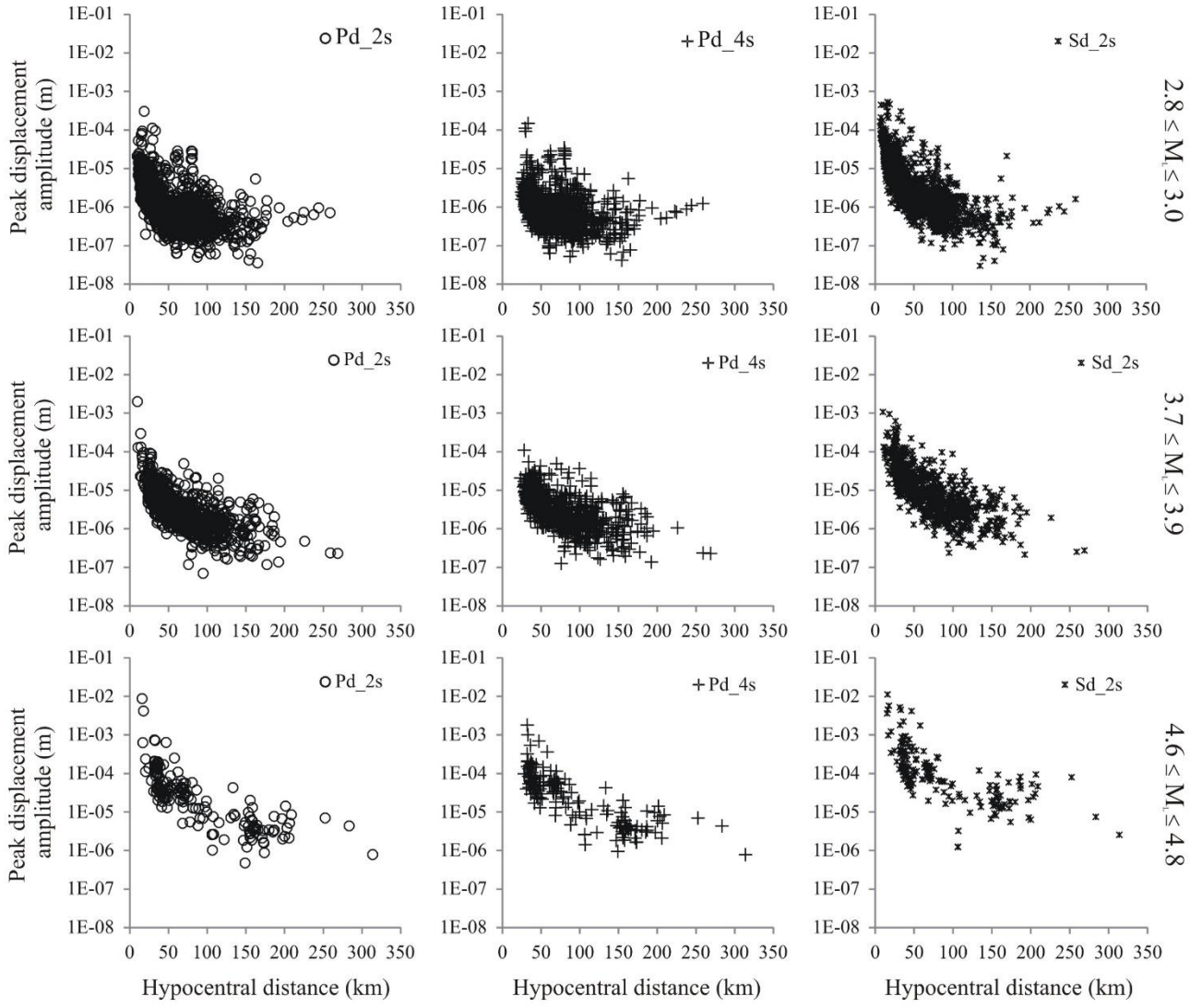


**Figure 4.** Plots of peak displacement amplitude versus hypocentral distance for three different range of magnitude.

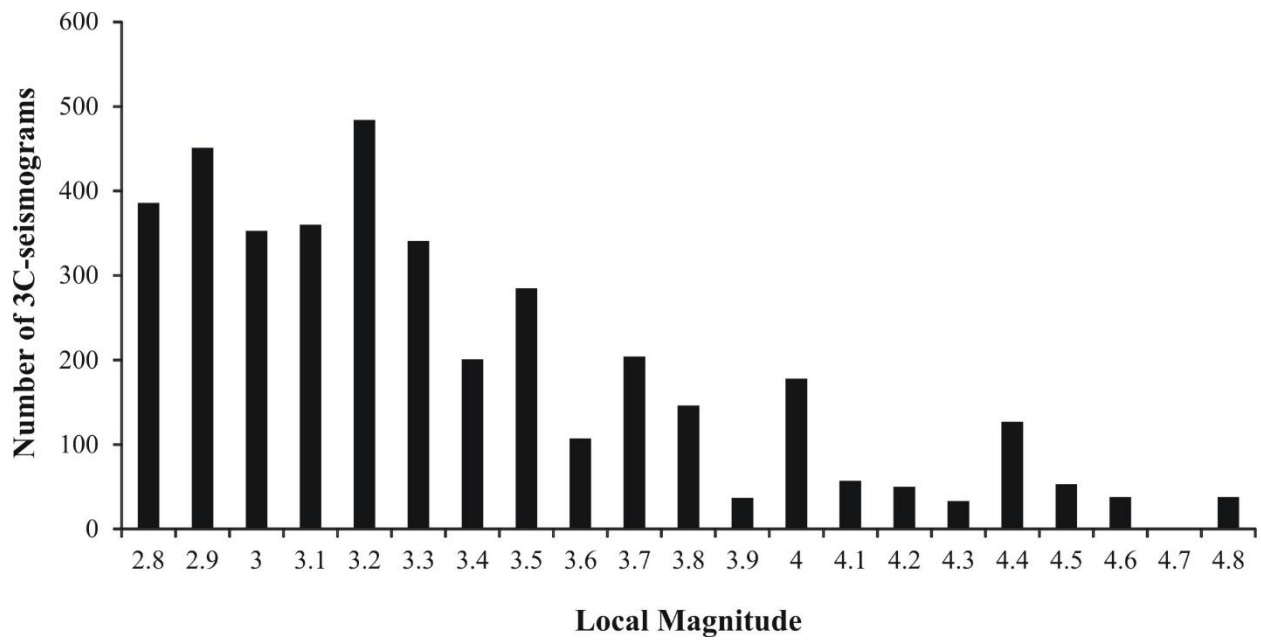


**Figure 5.** Number of 3C seismograms vs. local magnitude for the data set used to solve equation 2 (see text for details).

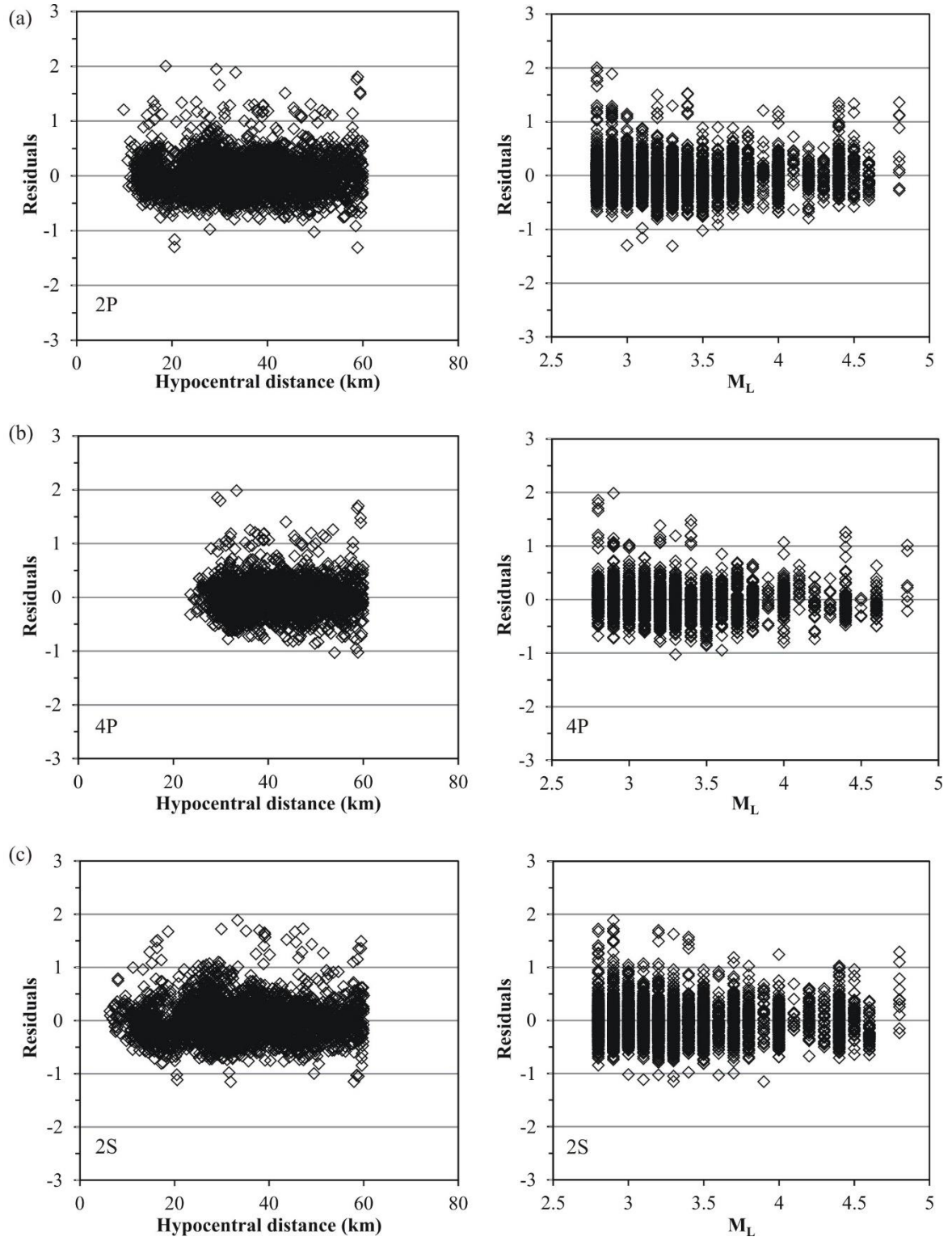


**Figure 6.** Distribution of residuals of the  $\text{Log}_{10}(P_d)$  as a function of the independent variables hypocentral distance and local magnitude for the three time windows (2P, 4P, and 2S).

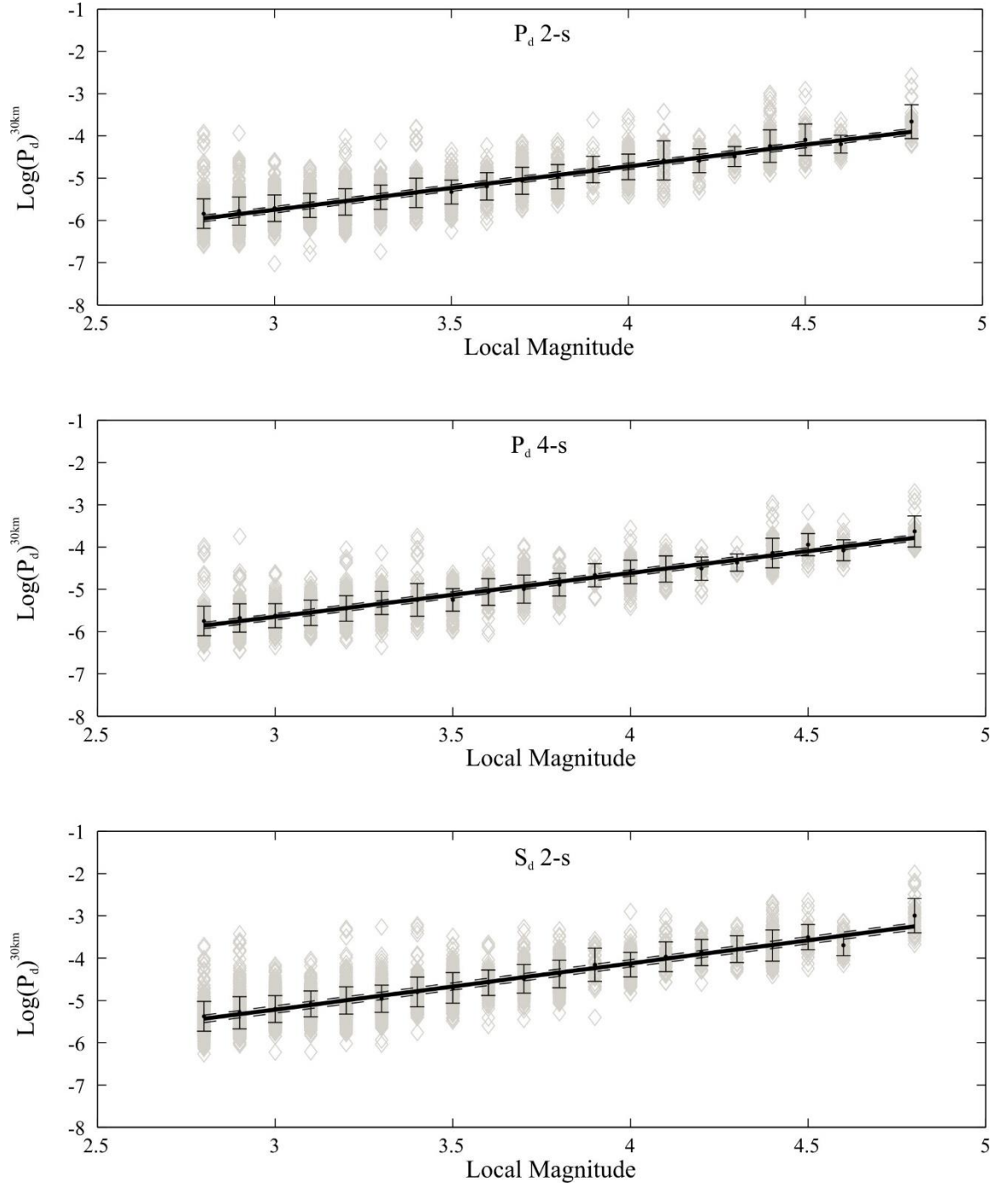


**Figure 7.** Logarithm of  $P_d$  parameter normalized at a reference distance of 30 km versus the local magnitude (a and b) in the time windows 2s and 4s from the P-onset and (c) 2s from the S-onset (grey diamonds). Black dots indicate the mean of  $\text{Log}_{10}(P_d)^{30km}$  for each  $M_L$  value plotted with its standard deviation. The solid and dashed lines represent the best fit and  $\pm 1WSE$  error bounds, respectively.

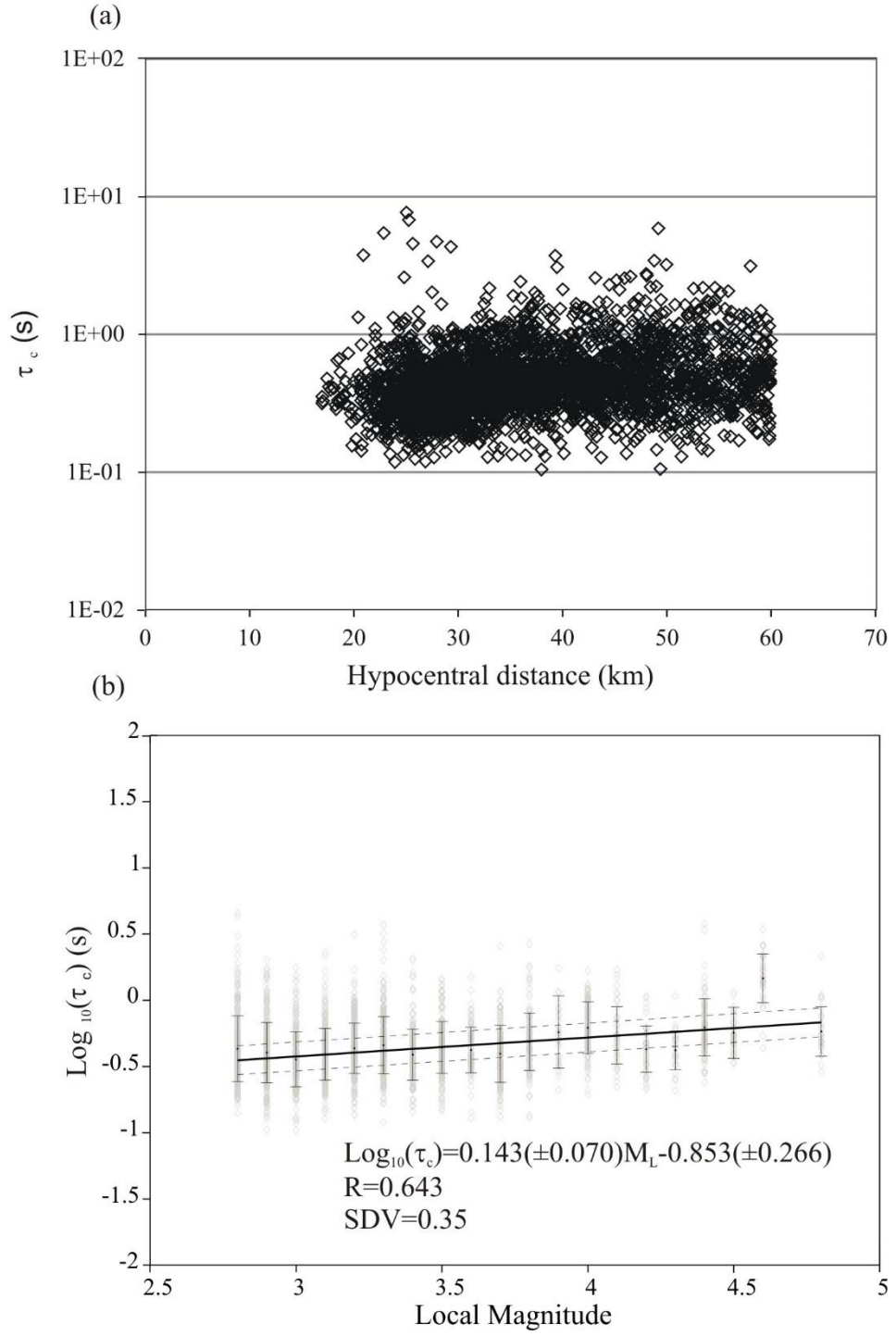


**Figure 8.** (a) The  $\tau_c$  parameter versus hypocentral distance. (b) Correlation between the logarithm of period parameter  $\tau_c$  value and local magnitude (grey diamonds). Black dots indicate the mean of  $\text{Log}_{10}(\tau_c)$  for each local magnitude value plotted with its standard deviation. The best fit regression line (solid line), along with  $\pm 1WSE$  error bounds (dashed lines), is shown.  $R$  is the correlation coefficient.

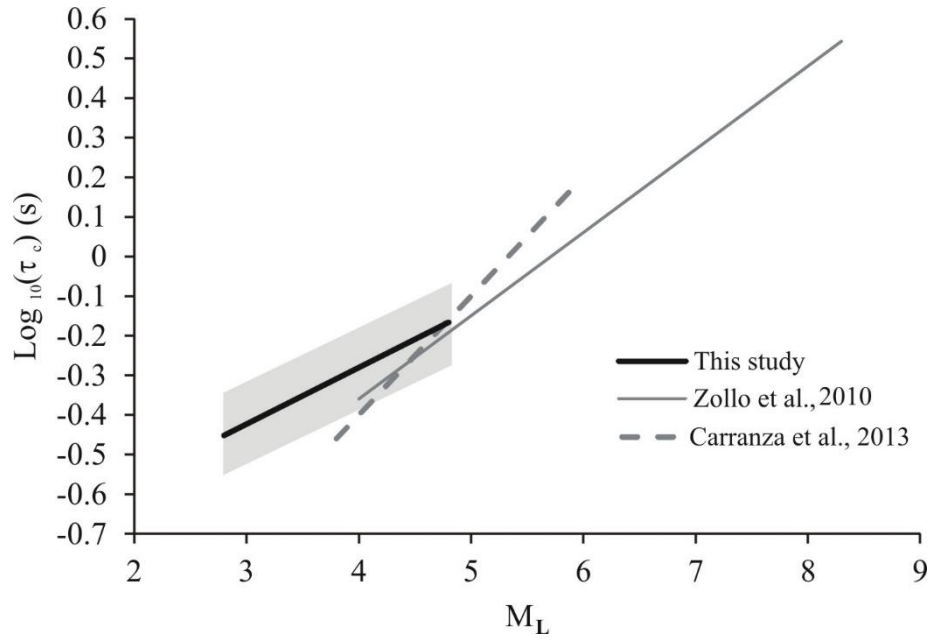


**Figure 9.**  $\tau_c$ -magnitude relations obtained from this study, from Zollo *et al.* (2010), and Carranza *et al.* (2013). The grey area indicates the  $\pm 1SDV$  error bounds.



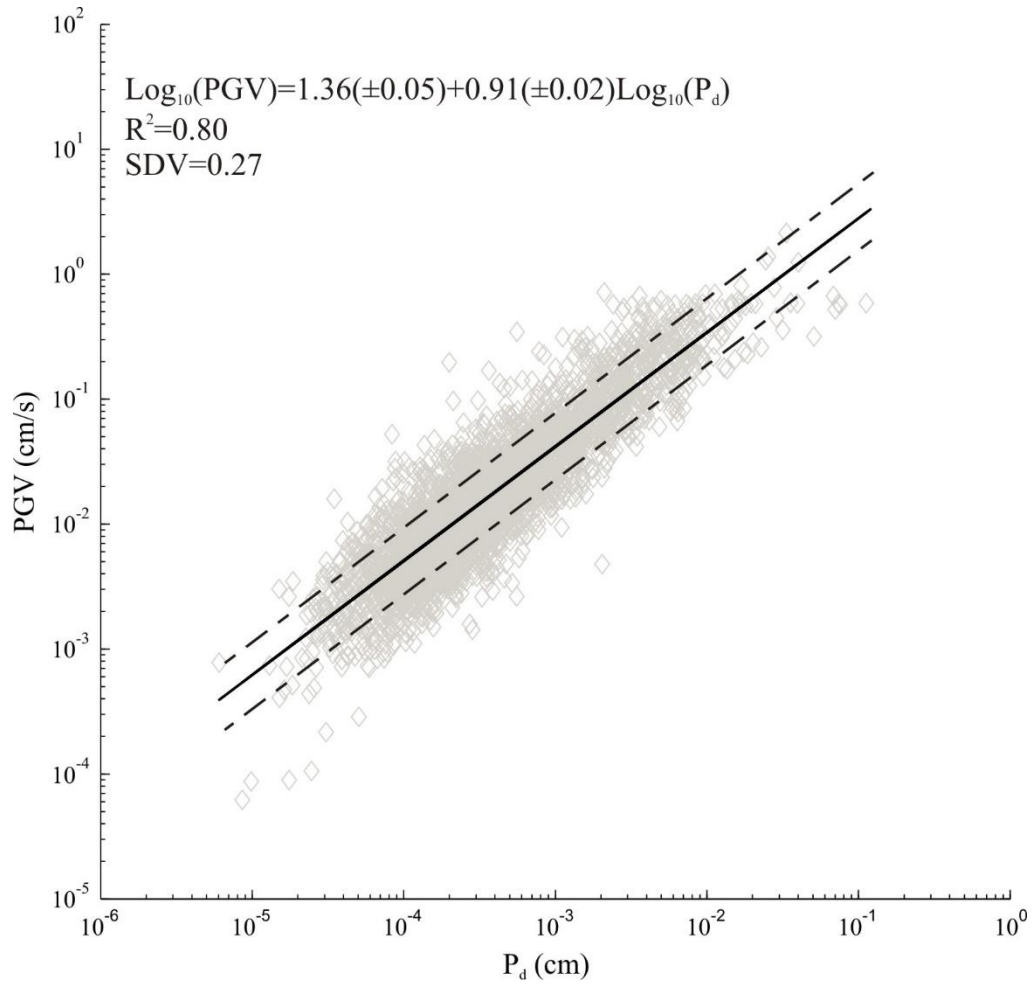


**Figure 10.** Peak ground velocity (*PGV*) versus peak initial displacement amplitude (*P<sub>d</sub>*) for hypocentral distances up to 60 km. Solid and dashed lines show the least squares fit and the range of one standard deviation, respectively. *R* is the correlation coefficient and *SDV* is the standard deviation.

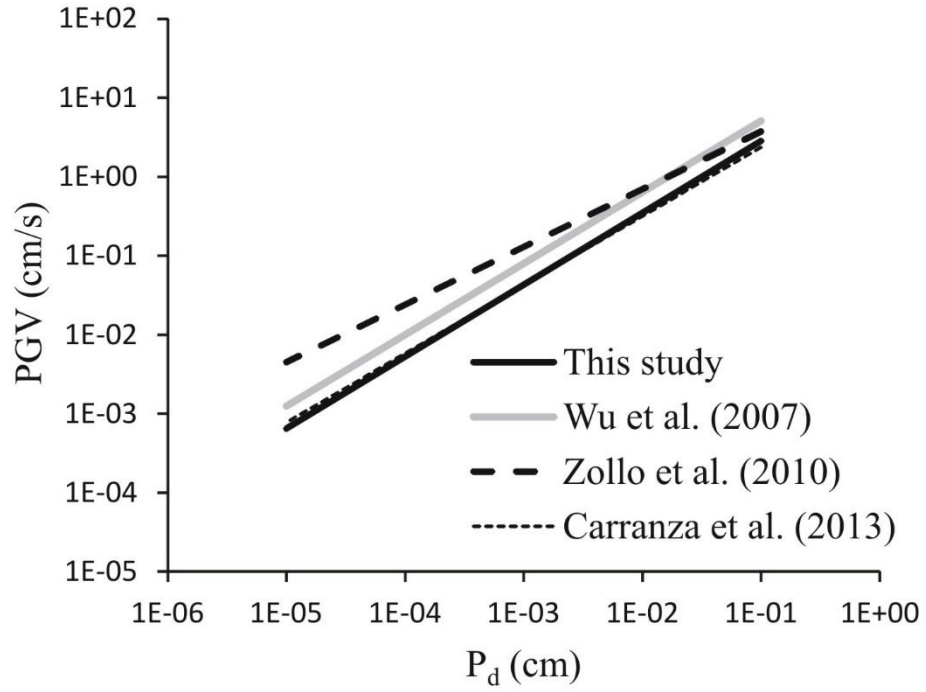


**Figure 11.** Comparison of  $PGV-P_d$  relationship obtained in this study with those estimated by Wu *et al.* (2007) (data from Taiwan and Southern California), Zollo *et al.* (2010) (data from Japan, Taiwan and Italy), and Carranza *et al.* (2013) (data from south of Iberian Peninsula).

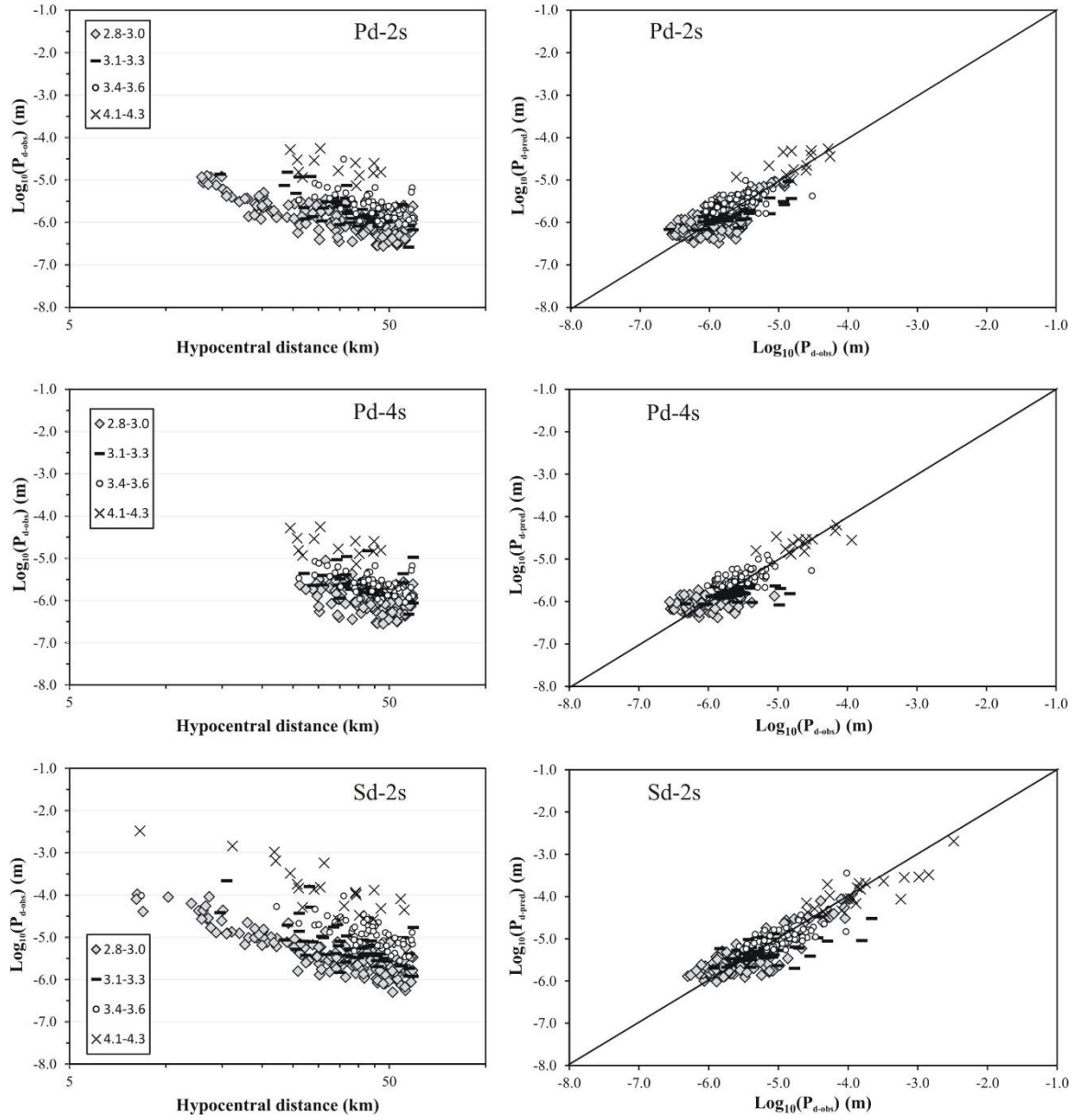


**Figure 12.** (Left) Plots of observed values of  $\text{Log}_{10}(P_d)$  versus the hypocentral distance. (Right) Plots of predicted values of  $\text{Log}_{10}(P_d)$  versus the observed ones (the line 1:1 is also shown) from the three time windows (2P, 4P, and 2S) for the 20 selected events (see also Table 3) of the test dataset.

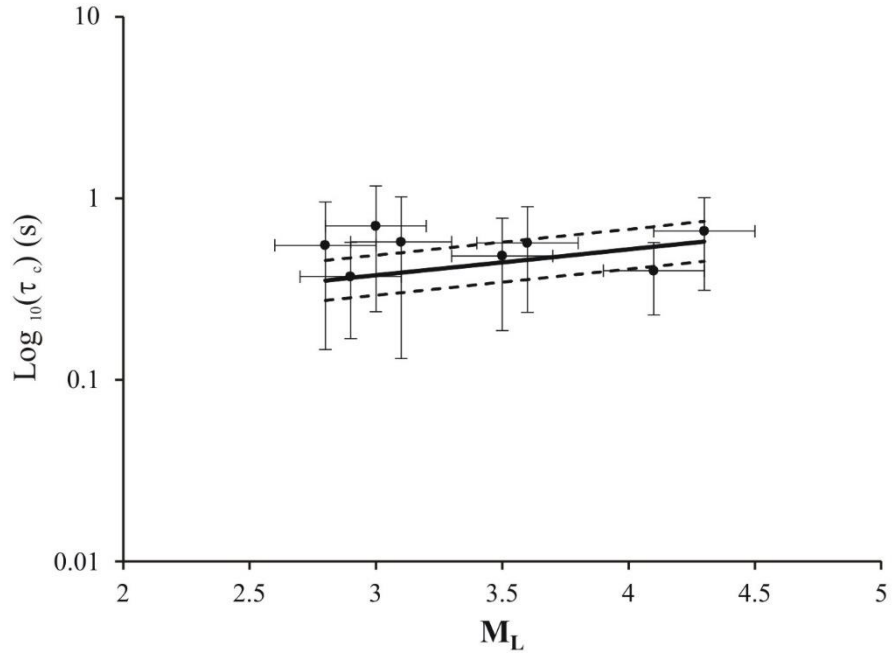


**Figure 13.** The observed  $\tau_c$  parameter versus the local magnitude ( $M_L$ ) for the 20 seismic events belonging to the test dataset. The predicted  $\tau_c$  (black line) by equation (7) and  $\pm 1SVD$  (black dashed lines) are also shown.

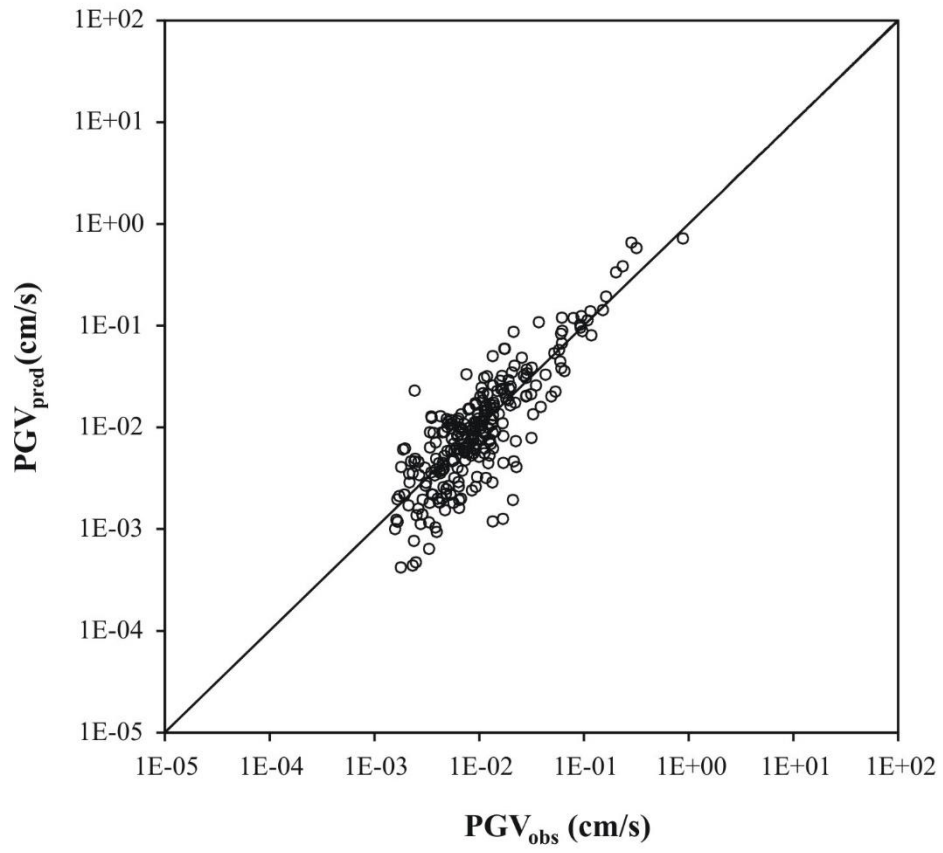


**Figure 14.** Predicted  $PGV$  ( $PGV_{pred}$ ) versus observed  $PGV$  ( $PGV_{obs}$ ) for the 20 selected events of test dataset (see text for details). The line 1:1 is also shown.

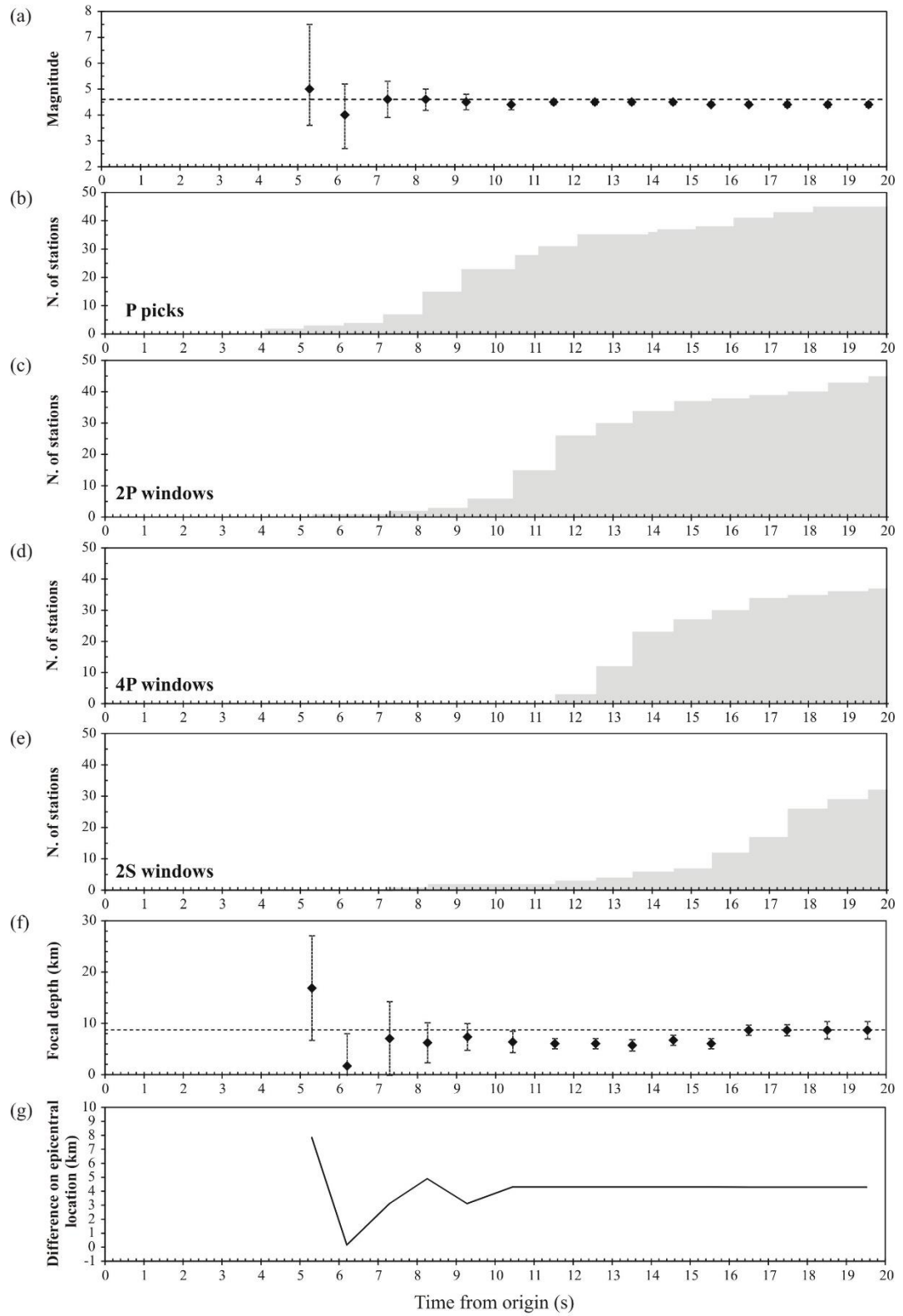


**Figure 15.** PRESTo timeline for the  $M_L$  4.6, 23 June 2011 earthquake occurring near the village of Tortorici. The dashed line in the plots (a) and (f) represent the reference magnitude and focal depth, respectively, obtained from the seismic catalog.

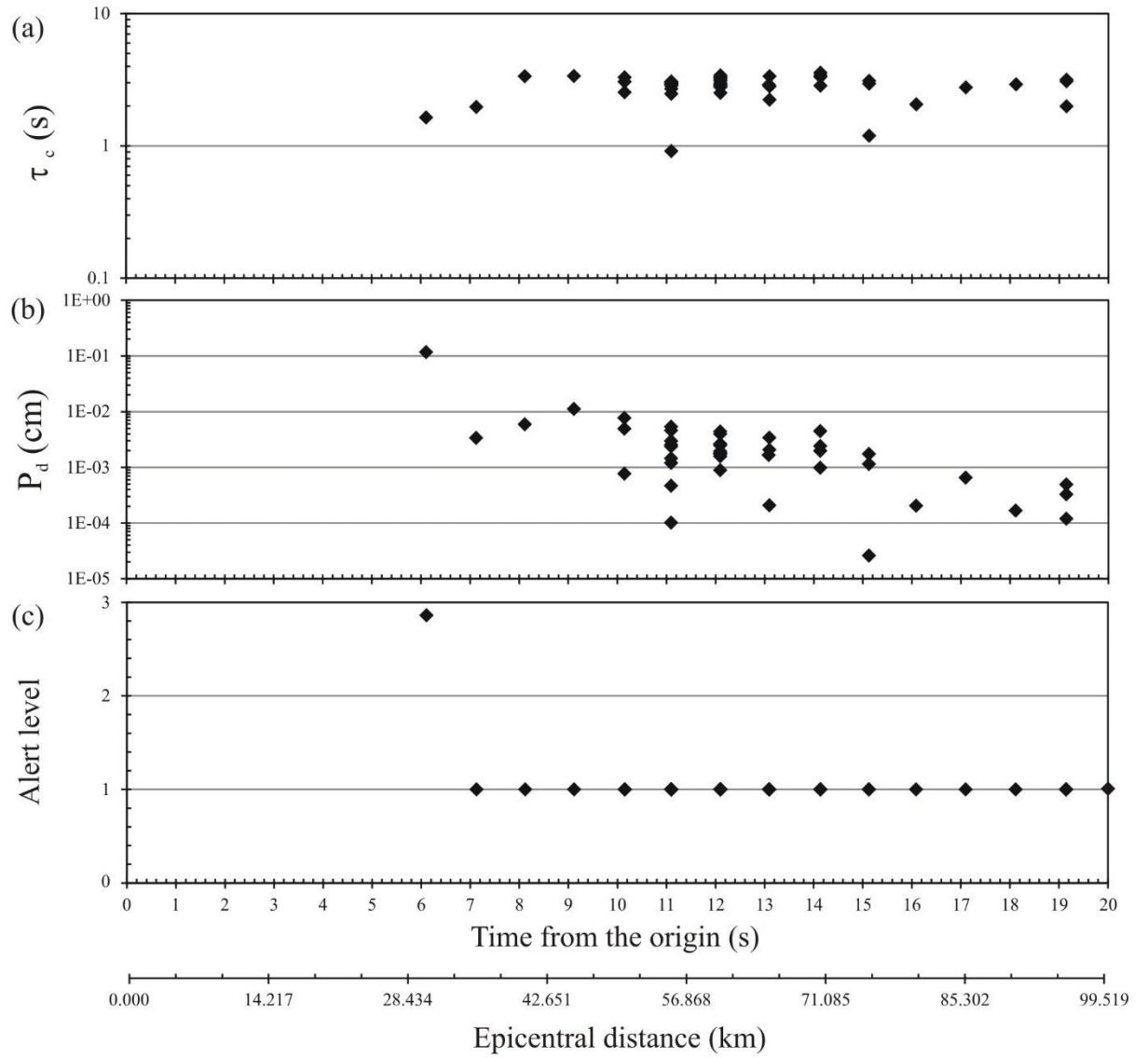


**Figure 16.** Evolution in time of the ground parameters (a)  $\tau_c$ , (b)  $P_d$ , and (c) the corresponding alert level at the different stations for the  $M_L$  4.6, 23 June 2011 earthquake as estimated by the code PRESTo.



*Bulletin of the Seismological Society of America*

## COPYRIGHT/PUBLICATION-CHARGES FORM

PLEASE FILL OUT AND SUBMIT THIS FORM ONLINE WHEN SUBMITTING YOUR PAPER  
OR FAX IT TO FAX NUMBER 503 405 7190

Manuscript Number: BSSA-D- \_\_\_\_\_ [leave blank for new submissions]

Title: ESTIMATION OF EARTHQUAKE EARLY WARNING PARAMETERS FOR EASTERN SICILY

Authors: GIUSEPPINA TUSA, CARLA YUSUMECI, DOMENICO PATANE

**COPYRIGHT**

In accordance with Public Law 94-533, copyright to the article listed above is hereby transferred to the Seismological Society of America (for U.S. Government employees, to the extent transferable) effective if and when the article is accepted for publication in the *Bulletin of the Seismological Society of America*. The authors reserve the right to use all or part of the article in future works of their own. In addition, the authors affirm that the article has not been copyrighted and that it is not being submitted for publication elsewhere.

To be signed by at least one of the authors (who agrees to inform the others, if any) or, in the case of "work made for hire," by the employer.



Authorized Signature for Copyright

GIUSEPPINA TUSA

Print Name (and title, if not author)

July 19, 2016

Date

**PUBLICATION CHARGES**

The Seismological Society of America requests that institutions supporting research share in the cost of publicizing the results of that research. The Editor has the discretion of waiving publication charges for authors who do not have institutional support. In addition to regular publication charges there is a nominal fee for publishing electronic supplements. Current rates are available at <http://www.seismosoc.org/publications/journal-publication-charges/>.

**Color options:** Color figures can be published (1) in color both in the online journal and in the printed journal, or (2) in color online and gray scale in print. Online color is free; authors will be charged for color in print. You must choose one option for all of the color figures within a paper; that is, you cannot choose option (1) for one color figure and option (2) for another color figure. You cannot submit two versions of the same figure, one for color and one for gray scale. You are responsible for ensuring that color figures are understandable when converted to gray scale, and that text references and captions are appropriate for both online and print versions. Color figures must be submitted before the paper is accepted for publication.

Art guidelines are at <http://www.seismosoc.org/publications/bssa/bssa-art-submission-guidelines/>

Will publication charges be paid? Check one:

☐ **BOTH PUBLICATION CHARGES AND COLOR CHARGES WILL BE PAID**, and all color figures for this paper will be color both online and in print. This option requires full payment of publication & color charges.

☒ **ONLY PUBLICATION CHARGES WILL BE PAID**, and all figures for this paper will be gray scale in print. Color figures, if any, will be color online.

☐ **REQUEST A REDUCTION IN PUBLICATION CHARGES.** Send a letter of request and explanation to the Editor-in-Chief at [BSSA@seismosoc.org](mailto:BSSA@seismosoc.org). Color figures, if any, will be color online but grey scale in print.

Send Invoice to: ISTITUTO NAZIONALE DI GEOFISICA E VOLCANOLOGIA -  
SEZIONE DI CATANIA, PIAZZA BOCA 2, 95125 CATANIA, ITALY

If your paper is accepted for publication, SSA requires that you fill out and submit an online billing/offprint form.

Questions regarding billing should be directed to the SSA Business Office,  
400 Evelyn Avenue, Suite 201 Albany, CA 94706 USA Phone 510 525-5474 Fax 510 525-7204